

REPORT DOCUMENTATION PAGE

Form Approved
OMB NO. 0704-0188

Public Reporting burden for this collection of information is estimated to average 1 hour per response, including the time for reviewing instructions, searching existing data sources, gathering and maintaining the data needed, and completing and reviewing the collection of information. Send comment regarding this burden estimates or any other aspect of this collection of information, including suggestions for reducing this burden, to Washington Headquarters Services, Directorate for Information Operations and Reports, 1215 Jefferson Davis Highway, Suite 1204, Arlington, VA 22202-4302, and to the Office of Management and Budget, Paperwork Reduction Project (0704-0188), Washington, DC 20503.

1. AGENCY USE ONLY (Leave Blank)		2. REPORT DATE 4/30/98		3. REPORT TYPE AND DATES COVERED 7/15/94 - 12/31/98	
4. TITLE AND SUBTITLE Rigorous Analysis of Large Scale MMIC Circuit Devices				5. FUNDING NUMBERS DAAH04-94-G-0243	
6. AUTHOR(S) Stephen Gedney					
7. PERFORMING ORGANIZATION NAME(S) AND ADDRESS(ES) University of Kentucky, Department of Electrical Engineering 453 Anderson Hall, Lexington, KY 40506-0046				8. PERFORMING ORGANIZATION REPORT NUMBER	
9. SPONSORING / MONITORING AGENCY NAME(S) AND ADDRESS(ES) U. S. Army Research Office P.O. Box 12211 Research Triangle Park, NC 27709-2211				10. SPONSORING / MONITORING AGENCY REPORT NUMBER ARO 3349.8-EL-DPS	
11. SUPPLEMENTARY NOTES The views, opinions and/or findings contained in this report are those of the author(s) and should not be construed as an official Department of the Army position, policy or decision, unless so designated by the documentation.					
12 a. DISTRIBUTION / AVAILABILITY STATEMENT Approved for public release; distribution unlimited.				12 b. DISTRIBUTION CODE	
13. ABSTRACT (Maximum 200 words) The focus of this research has been on the development of scalable time-dependent solutions of Maxwell's equations for the analysis of printed microwave circuits. The planar generalized Yee (PGY) algorithm has been developed which is an explicit scheme based on an unstructured grid with planar symmetry. Implicit finite element schemes have also been investigated. Radiation boundaries are enforced using the newly developed uniaxial perfectly matched layer (UPML). It is shown that the PML can be perfectly matched to a general lossy inhomogeneous media, as well as dispersive, nonlinear and anisotropic media providing high levels of absorption. The means of efficiently modeling infinitely periodical geometries using orthogonal and nonorthogonal finite difference time domain (FDTD) methods is also introduced. Finally, modeling linear and nonlinear devices within the FDTD and PGY methods using a state variable solution is presented. Examples of a linear amplifier, a nonlinear diode and nonlinear amplifier are presented.					
14. SUBJECT TERMS				15. NUMBER OF PAGES	
				16. PRICE CODE	
17. SECURITY CLASSIFICATION OR REPORT UNCLASSIFIED	18. SECURITY CLASSIFICATION ON THIS PAGE UNCLASSIFIED	19. SECURITY CLASSIFICATION OF ABSTRACT UNCLASSIFIED	20. LIMITATION OF ABSTRACT UL		

NSN 7540-01-280-5500

Standard Form 298 (Rev.2-89)
Prescribed by ANSI Std. Z39-18
298-102

DTIC QUALITY INSPECTED 8

Enclosure 1

19980519 123

RIGOROUS ANALYSIS OF LARGE SCALE MMIC CIRCUIT DEVICES

FINAL PROGRESS REPORT

STEPHEN D. GEDNEY

APRIL 1998

U.S. ARMY RESEARCH OFFICE

GRANT# DAAHO4-94-G-0243

**DEPARTMENT OF ELECTRICAL ENGINEERING
UNIVERSITY OF KENTUCKY
LEXINGTON, KY 40506-0046**

**APPROVED FOR PUBLIC RELEASE;
DISTRIBUTION UNLIMITED.**

**THE VIEWS, OPINIONS, AND/OR FINDINGS CONTAINED IN THIS
REPORT ARE THOSE OF THE AUTHOR AND SHOULD NOT BE
CONSTRUED AS AN OFFICIAL DEPARTMENT OF THE ARMY
POSITION, POLICY OR DECISION, UNLESS SO DESIGNATED BY
OTHER DOCUMENTATION**

TABLE OF CONTENTS

<u>Section</u>	<u>Page</u>
3. LIST OF FIGURES AND TABLES	iv
4. STATEMENT OF THE PROBLEM	1
5. SUMMARY OF IMPORTANT RESULTS	3
I. Accomplishments	3
II. Explicit Generalized Yee-Algorithm	5
III. Well Posed Non-Orthogonal FDTD Methods	8
1. Well Posedness	8
2. Validation	11
IV. Uniaxial Perfectly Matched Layer Truncation of Computational Space for Simulation of Unbounded Domains	13
1. Introduction	13
2. The Uniaxial PML	13
3. Matching PML to Generalized Media	15
4. Reflection Error	17
5. Validation	19
V. Parallel Finite-Element Frequency-Domain Method	26
1. Introduction	26
2. Formulation	27
3. Finite Element Tearing and Interconnecting Method	27
4. Results	29
VI. A Parallel Unconditionally Stable Finite-Element Time-Domain Algorithm	32
VII. Orthogonal and Nonorthogonal FDTD Analysis of Periodic Structures	35
1. Introduction	35
2. Formulation	35
3. Orthogonal Grid FDTD	36
4. Non-Orthogonal Grid FDTD	38
5. UPML Boundary Condition	39
6. Validation	39
VIII. Incorporating the State Variable Technique into the FDTD and PGY Methods for Modeling Linear and Nonlinear Devices	42
1. Introduction	42
2. The Current-Source Approach	43
3. State-Variable Solution	43
4. Linear Loads	46
5. Nonlinear Loads	48

6. LIST OF PUBLICATIONS	54
7. SCIENTIFIC PERSONNEL	56
8. REPORT OF INVENTIONS	56
9. BIBLIOGRAPHY	57

List of Figures and Tables

<u>Figure</u>	<u>Page</u>
Fig. 1	Ka-band Wilkinson power divider (32 GHz). <i>Source:</i> S. Gedney and F. Lansing, IEEE Transactions on Microwave Theory and Techniques.....6
Fig. 2	Magnitude of the S-parameters of a Wilkinson power divider computed using the PGY and the FD-TD methods. (a) $ S_{21} $. (b) $ S_{21} $. <i>Source:</i> S. Gedney and F. Lansing, IEEE Transactions on Microwave Theory and Techniques.....7
Fig. 3	Abrupt Transition from 50 Ω GCPWG to 50 Ω microstrip to 50 Ω GCPWG printed on a 25 mil Alumina Substrate. (a) Cross section of the GCPWG circuit with 50 mil spaced vias. (b) Top view of the abrupt transition (fabricated by Hughes Aircraft).7
Fig. 4	Computed and Measured S-parameters for a GCPWG - microstrip transition (Measurements by Hughes Aircraft).....7
Fig. 5	Dielectric ring in a rectangular PEC cavity ($a = 324$ mm, $b = 121$ mm, $c = 43$ mm. The ring is centered at $w_1 = 207.25$ mm, $w_2 = 116.75$ mm, $b/2$ along the y -direction and rests on the ground plane. The ring has a height of $h = 39$ mm, inner radius $r_1 = 16.65$ mm, and outer radius $r_2 = 26.75$ mm.)12
Fig. 6	TE-polarized wave excited by a vertically directed electric current source in a two-dimensional region. The working volume is 40 mm x 40mm, and is surrounded by PML layers of thickness d . The source is located at the center of the region. The fields are probed at two observation points A and B22
Fig. 7	Relative error at points A and B over 1,000 time iterations for 5 and 10 cell thick PMLs terminating a 40 x 40 cell lattice excited by a small dipole with $\sigma_{\max} = \sigma_{opt}$ and $\kappa = 1$22
Fig. 8	Maximum relative error due to a 5 and 10 cell thick PML termination of a 40 x 40 cell lattice excited by a small dipole over 1,000 time iterations versus $\sigma_{\max}/\sigma_{opt}$ ((7.67)). Polynomial spatial scaling with $m = 4$ and $\kappa = 1$23
Fig. 9	Maximum relative error due to a 15 thick PML termination of a 40 x 40 cell lattice excited by a small dipole over 1,000 time iterations versus $\sigma_{\max}/\sigma_{opt}$ ((7.67)). Polynomial spatial scaling with $m = 4$ and $\kappa = 1$23
Fig. 10	Contour plot of the maximum relative error at points A and B , respectively, due to a polynomial scaled 10 cell thick PML termination of a 40 x 40 cell lattice excited by a small dipole over 1,000 time iterations versus $\sigma_{\max}/\sigma_{opt}$ and m24
Fig. 11	Maximum relative error at points A and B , respectively, due to a geometrically scaled 10 cell thick PML termination of a 40 x 40 cell lattice excited by a small dipole over 1,000 time iterations versus g and $\ln(R(0))$24

Fig. 12	$ S_{11} $ of a microstrip fed patch antenna (superimposed) printed on a 31.25 mil Duroid substrate($\epsilon_r = 2.2$) computed via the FDTD method. The FDTD lattice is terminated by a 10-cell thick uniaxial PML layer which is placed: — \times — 3 cells from the edge of the patch and 5 cells above the patch, and — \square — 10 cells from the edges of the patch. <i>Source: Gedney, IEEE Transactions on Antennas and Propagation</i> , vol. 44, pp. 1630-1639, December 1996.....	25
Fig. 13.	Fitted reflection error for a 0.4m x 0.4m x 1.1m waveguide with a 0.4m PML for different values of the polynomial variation, m, and σ_{\max} within the PML.	31
Fig. 14	A PEC Wedge in a cavity	33
Fig. 15	Tetrahedral mesh of the surface of the wedge and cavity	33
Fig. 16	Variation of resonant frequency v/s the time step.....	33
Fig. 17	Variation of Execution time and Average number of CG iterations per time step with the time step.	34
Fig. 18	Cross-section of a slab of two-dimensional photonic band-gap material.....	40
Fig. 19	Transmission coefficient of four rod deep photonic bandgap structure for a TM_z plane wave incident at 20 degrees. (a) magnitude, (b) phase. Periodic cell is 9mm wide and rod diameter is 4 mm, and $\epsilon_r = 4.2$	41
Fig. 20	Equivalent circuit for the current-source state variable model.	50
Fig. 21	The small signal equivalent circuit model used for the GaAs MESFET amplifier.....	51
Fig. 22	The layout for the MESFET amplifier. The microstrips have 50 Ω characteristic impedances and are printed on a 31 mil substrate with $\epsilon_r = 2.23$. The FDTD model had a spatial discretization of $\Delta x = \Delta y = 0.3000875$ mm, $\Delta z = 0.15748$ mm, and a time step of $\Delta t = 4.011 \times 10^{-13}$ s was used. This lead to 8 cells across the microstrip width and 5 cells through the substrate.	51
Fig. 23	The magnitude of the S-parameters of the linear MESFET amplifier computed by FDTD with the state-variable model and compared by computations using HP-EESOF TM ,	52
Fig. 24	Equivalent circuit for the diode model. Both C_{pack} and L_{pack} are introduced to model parasitic packaging affects.	52
Fig. 25	Voltage across the nonlinear diode terminating a 50 ohm microstrip line.	53
Fig. 26	The magnitude of the S-parameters computed by the FDTD simulation for the nonlinear MESFET amplifier.....	53

Table 1	Resonant Frequencies of the Dielectric Ring Loaded Cavity, $\epsilon_r = 2.06$	12
Table 2	Resonant Frequencies of the Dielectric Ring Loaded Cavity, $\epsilon_r = 9.8$	12
Table 3	Comparison of results for the FETI algorithm with 3072 cells per Processor.....	31
Table 4	Results for waveguide problem on a Single Processor using Diagonal Preconditioning.	31

4. STATEMENT OF THE PROBLEM STUDIED

In the last decade, MMICs have played a leading role in the design of microwave communications systems. As the fabrication technologies of these devices have matured, both military and commercial applications have demanded smaller and denser MMICs operating over larger bandwidths and at higher operating frequencies (into the K_a and U bands). This has led to an increased need for more rigorous analyses that explicitly model the electromagnetic interactions within these devices. Although, it is instructive to isolate each element of the MMIC and analyze them independently, proper characterization of densely packaged circuits require the rigorous analysis of entire circuits simultaneously, or large blocks of circuits. Specifically, electromagnetic effects such as coupling, radiation, surface waves, and other affects that lead to induced signals on neighboring signal lines need be accounted for to accurately characterize the circuit devices.

The objective of this research has been to develop a MMIC circuit simulator based on direct time-domain solutions of Maxwell's equations. The simulator is capable of analyzing MMICs using either the traditional finite-difference time-domain (FDTD) method, an explicit planar generalized Yee-algorithm (PGY) based on generalized unstructured grids, or the implicit Finite Element Time-Domain (FETD) method. The FDTD method is a highly robust and efficient computational method that is well suited for circuits whose geometries are separable in a Cartesian coordinate system. The PGY and the FETD methods, which are based on volume discretizations using unstructured grids, are much better suited for analyzing circuits with complex geometries. The FETD offers a higher-order approximation of the fields. Furthermore, it can be posed in a form that is unconditionally stable. As a result, the time step is not restricted by a Courant limit. Unfortunately, in many applications it is still more computationally intensive than the PGY method since it requires a sparse matrix solution required at each time iteration.

In the course of the development of these algorithms, it was found that most non-orthogonal FDTD methods, including locally-deformed FDTD methods, non-orthogonal FDTD methods, and the PGY method, suffer from late time instability. Typically, these late time-instabilities will corrupt the analysis of large resonant structures requiring large numbers of time steps. Upon investigating, it was found that these algorithms are not well posed. Subsequently, a sufficient test for well-posedness was developed. Secondly, methods were introduced that rendered these algorithms to be well posed were developed.

A second objective of the proposed research has been to develop efficient high-performance parallel algorithms for the implicit and explicit time-domain methods. Due to the characteristics of volume discretizations, the FDTD, PGY, and FETD methods can be extremely computationally intensive when solving large resonant structures. It has been shown that these algorithms have high degrees of parallelism, and very large problems can be efficiently analyzed on high-performance parallel algorithms. Explicit schemes, such as the FDTD and PGY methods, are most

efficiently parallelized using a divide and conquer scheme based on a spatial decomposition of the volume mesh. On the other hand, a divide and conquer approach, such as a spatial decomposition in conjunction with a parallel iterative linear system solution such as the Conjugate Gradient (CG) method, for implicit schemes such as the FETD is not necessarily optimal. This is because as the problem size increases, the condition number of the sparse matrix comensurately increases. Subsequently, the number of iterations required to converge at each time step grows with the problem size. A more efficient approach has been found that is based on the method of Lagrange multipliers. Specifically, a spatial decomposition is performed on the global mesh. Each subregion is then mapped to a processor and solved using a sparse direct solver locally. Constraints enforcing the continuity of the tangential fields are impressed across each interface using Lagrange multipliers, leading to a global linear system of equations. This method has been referred to as the Finite-Element Tearing and Interconnecting (FETI) algorithm. It has been found that this method actually results in super-linear speedups for the FETD algorithm due to the nature of the condition number of the linear system.

A final objective of the research has been to develop the capability of analyzing both linear and non-linear circuits. To this end, lumped circuit models have been introduced into the FDTD and PGY algorithms using a state variable technique. The state variable method allows for the inclusion of linear and non-linear devices to be directly incorporated into the FDTD and PGY simulations in a manner that is device independent. Specifically, a device library can be created such that the FDTD algorithm is independent of the device. Rather, the port voltages or currents are provided to the generic state variable model, and the output port currents or voltages are then returned to the FDTD method and then applied to the local fields.

Other subsequent venues have been pursued through the course of this research that have spawned from the development of the above algorithms. Initially, one limitation of finite methods such as FDTD or FETD is when solving unbounded problems, a mesh truncation condition must be introduced which efficiently and accurately terminates (or absorbers) all radiation incident upon an exterior boundary. For many applications, such as computing the DC bias of a non-linear FET device, traditional pseudo-differential based absorbing boundaries introduce significant error. Subsequently, alternative absorbing boundary conditions were pursued. This lead to the development of an anisotropic perfectly matched layer (PML) medium for the truncation of FDTD lattices. This method, which is very similar in characteristic to Berenger's split-field PML, is based on a physical interpretation of the perfectly matched layer medium as a uniaxial medium rather than a mathematical medium. This has lead to the immediate extension of the PML to inhomogeneous media, lossy media, dispersive media, and non-linear media.

Another development that has stemmed from this research is the development of an algorithm which extends FDTD and non-orthogonal FDTD to periodic structures. This work was initiated by

the Signature Technology Laboratory at Georgia Tech. Research Institute. The difficulty with existing periodic FDTD based algorithms was that they were inherently unstable. To circumvent this, a new algorithm based on a split-field formulation has been developed for both orthogonal and non-orthogonal FDTD methods that efficiently treats the scattering and radiation by periodic structures that is stable for all angles of incidence, and highly efficient.

5. SUMMARY OF IMPORTANT RESULTS

I. Accomplishments

As per meeting the objectives outlined in Section 4, a summary of the specific accomplishments of this research program are encapsulated as follows:

- 1) Development of the planar generalized Yee-algorithm (PGY), an explicit time-domain solution of Maxwell's equations that assumes a volume discretization based on an unstructured grid [1-5]. The PGY algorithm exploits the planar symmetry of microwave circuits composed of planar stratified circuits and vias to greatly reduce the memory overhead. This algorithm has been successfully applied to large circuits and antennas.
- 2) The development of a test of well-posedness for explicit time-dependent solutions of Maxwell's equations based on staggered grids. From this theory, well-posed PGY algorithms and non-orthogonal FDTD algorithms have been successfully derived.
- 3) The development of an unconditionally stable implicit finite-element time-domain (FETD) solution of the inhomogeneous vector wave equation [6, 7].
- 4) The development of a highly scalable parallel algorithms for the finite-difference time-domain (FDTD) method, the generalized Yee and PGY algorithms, and the FETD method [8-12].
- 5) The development of a scalable parallel algorithm for the solution of sparse matrices arising from the FEM discretization of the vector wave equation. The technique is based on the method of Lagrange Multipliers, and has been used for both frequency dependent [13] and time-dependent FEM simulations [7].
- 6) The development of a uniaxial perfectly matched layer medium (UPML) for the truncation of FDTD lattices. This technique provides absorption on the order of 90 dB over broad frequency bands. The UPML has been successfully applied to inhomogeneous media, lossy media, dispersive, and non-linear media [14, 15], as well as to the non-orthogonal FDTD algorithm [16], and the frequency-domain FEM method [13].
- 7) This work has helped to promote collaborative efforts with engineers at Hughes Aircraft Company, Georgia Tech Research Institute and the Jet Propulsion Laboratory.

- 8) This effort has supported 3 M.S. students, 2 Ph. D. students, and a post doctoral associate.
- 9) Based on this effort 12 journal articles and 5 book chapters have been published, 3 other journal articles are currently under review, and 12 papers have been published in the proceedings of International Symposia.

In the remainder of this report, summaries of these accomplishments are provided. Specifically, in Section II, the explicit planar generalized Yee-algorithm is summarized with some examples of a few of the many microwave circuits analyzed with this technique. Section III introduces the concept of well-posedness, and test for well posedness for general Yee schemes based on conformal and nonorthogonal grids. It is shown that originally posed algorithms such as the contour patch FDTD method, the nonorthogonal FDTD method, and the PGY method are actually ill-posed. Well-posed methods are proposed and demonstrated. Section IV summarizes the uniaxial PML method and its implementation within the FDTD method. It also demonstrates that the uniaxial PML can be used to match generalized inhomogeneous lossy media. Through validation its effectiveness and application within the FDTD method is presented.

Sections V and VI deal with implicit schemes based on the finite-element method (FEM). Section V presents a parallel frequency dependent FEM with a uniaxial PML mesh termination. The parallel scheme is based on the method of Lagrange multipliers and excellent speedups are recorded. This method is extended to an unconditionally stable implicit finite element time-domain (FETD) method in Section VI.

Section VII extends the nonorthogonal FDTD method to periodic structures. To this end, a stable FDTD analysis based on orthogonal grids is first introduced. The advantage of the method introduced is that it is inherently stable for all angles of incidence, unlike previous methods. This method is then extended further to a nonorthogonal grid FDTD method.

Finally, section VIII discusses the incorporation of linear and nonlinear lumped devices into FDTD and PGY simulations using the state variable methods. The application of a linear amplifier, a nonlinear diode, and a nonlinear amplifier are presented.

II. Explicit Planar Generalized Yee Algorithm

A number of explicit methods for the solutions of Maxwell's equations based on non-orthogonal structured [17, 18] and unstructured methods [1-5, 19] have been proposed. The planar generalized Yee-algorithm (PGY) algorithm [3-5] has the advantage that it models three-dimensional geometries with planar symmetry via a mesh that is fully unstructured along two-dimensional cross-sections and structured along the third dimension. The PGY algorithm is based on the discretization of Ampere's and Faraday's laws in their integral form by projecting the vector fields onto the edges of a dual, staggered unstructured grid. By exploiting planar symmetry, significant memory savings can be realized. Based on such a discretization of the fields, and employing a central difference approximation for the time-derivatives, an explicit time-marching solution for vector field updates can be derived. The matrices are highly sparse, although due to the unstructuredness of the grid they must be stored. Fortunately, due to the regularity of the grid along one dimension, only the matrices due to one layer of cells are actually stored. This greatly reduces the overall memory requirement. The explicit update scheme is then expressed as a linear operator as

$$d^{n+\frac{1}{2}} = d^{n-\frac{1}{2}} + \Delta t C_h A_b b^n \quad (1)$$

$$b^n = b^{n-1} - \Delta t C_e D_\epsilon A_d d^{n-\frac{1}{2}} \quad (2)$$

where b and d are the vector of discrete vector flux densities associated with the primary and secondary cell faces, respectively, the superscripts refer to discrete time, C_e and C_h represent the discrete contour integrals of the electric and magnetic fields about primary and secondary cell faces, respectfully, D_ϵ is a diagonal matrix with entries representing the inverse of the relative permittivity, and A_b and A_d are the projection matrices. The role of the projection matrices are to project the normal face fields onto the dual edges passing through the faces. Note that for simplicity the domain is assumed to be lossless and non magnetic. The explicit field updates provide an extremely efficient computational technique that is second-order accurate for the simulation of the time-varying fields, and is stable, providing the time step satisfies the stability criterion [3-5].

An example of the simulation of a fields within a Wilkinson power divider is first presented. Figure 1 illustrates the geometry of a Wilkinson power divider designed for 3 dB power division (equal phase) at 32 GHz that is matched to 50 Ω microstrip lines. A 100 Ω chip resistor is placed between ports 2 and 3 for isolation. The microstrip device is printed on a 15 mil TMM substrate ($\epsilon_r = 3.25$) that is backed by a ground plane. A two-dimensional unstructured mesh used to analyze this circuit consisted of roughly 3200 arbitrarily shaped quadrilaterals. Along the vertical direction, the resultant 3-dimensional mesh was 25 cells high (uniformly spaced). The fields on the exterior boundary are updated using the second-order Higdon boundary condition. Figure 2

illustrates the S-parameters S_{11} and S_{21} computed for this device using the PGY-algorithm. It is noted that $S_{31} = S_{21}$ due to geometric symmetry. These results are also compared with simulated results using the FD-TD algorithm. The FD-TD model of the Wilkinson power divider was based on a uniform orthogonal grid ($\Delta x = 0.0573$ mm, $\Delta y = 0.0573$ mm, and $\Delta z = 0.0635$ mm). The curved boundaries were approximated by a staircase approximation, resulting in discretization error. Furthermore, due to the uniformity of the grid, the length of the quarter-wave transformers (the curved sections) were slightly lengthened. The combination of these lead to an upward shift in the resonant frequency and the other deviations from the PGY simulated results.

As a second example, consider the simulation of a transition from a 50 Ω grounded coplanar waveguide (GCPWG) to a 50 Ω microstrip line. The structure was printed on a 25 mil Alumina substrate, and the GCPWG consisted of a center conductor that was 10 mils wide, two symmetric outer fins 40 mils wide, with a gap of 5 mils between the center strip and the outer fins (see Fig. 3). Circular vias spaced 50 mils on center interconnected the fins to the ground plane. Figure 4 illustrates a comparison of results simulated using the PGY algorithm with measured results performed by Hughes Aircraft Company. Overall, good agreement is observed. It is noted that the PGY simulation assumed a lossless structure, where ~ 0.6 dB of conduction loss at 18 GHz is expected in S_{21} .

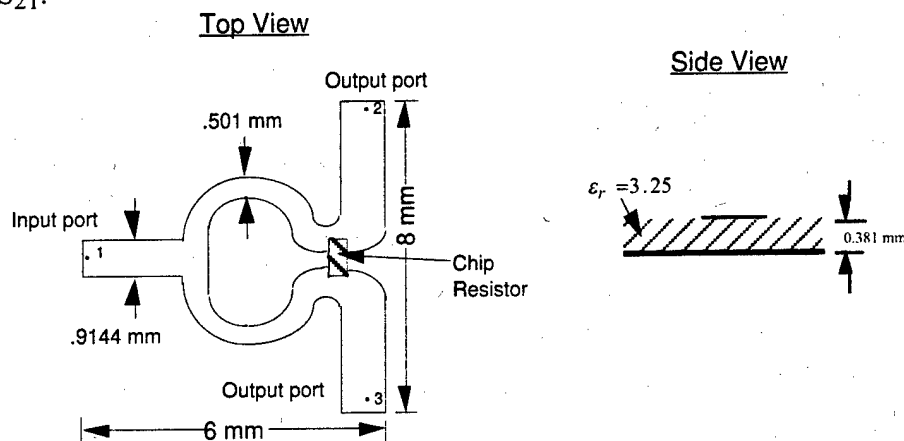


Fig. 1 Ka-band Wilkinson power divider (32 GHz). *Source:* S. Gedney and F. Lansing, IEEE Transactions on Microwave Theory and Techniques.

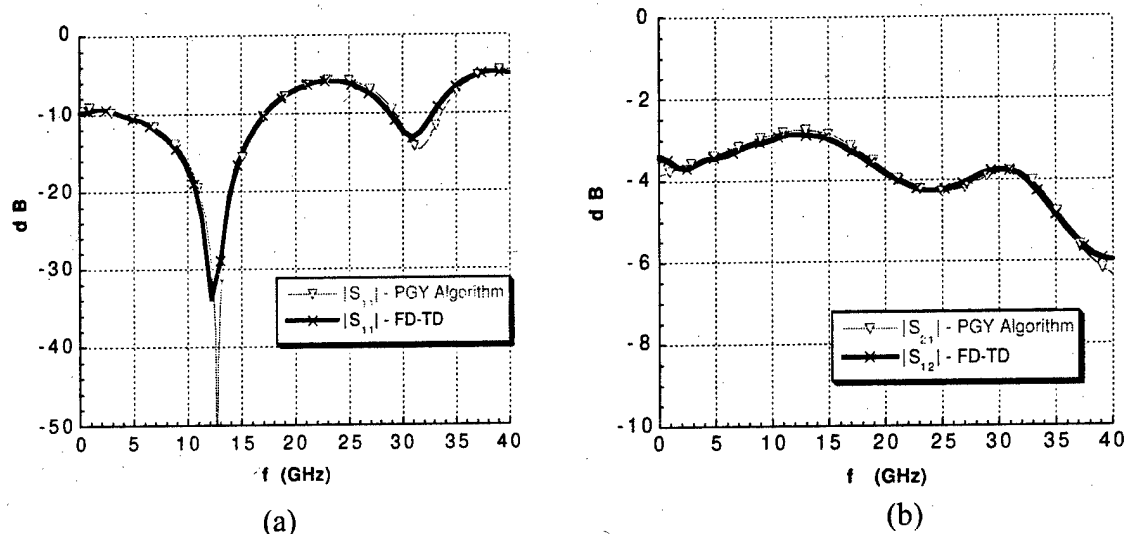


Fig. 2 Magnitude of the S-parameters of a Wilkinson power divider computed using the PGY and the FD-TD methods. (a) $|S_{11}|$. (b) $|S_{21}|$. Source: S. Gedney and F. Lansing, IEEE Transactions on Microwave Theory and Techniques.

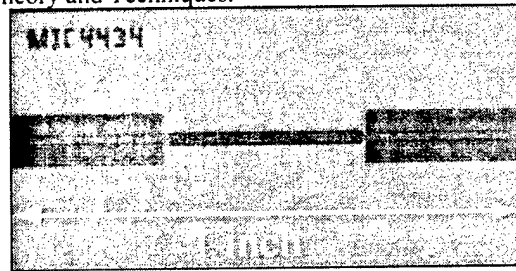
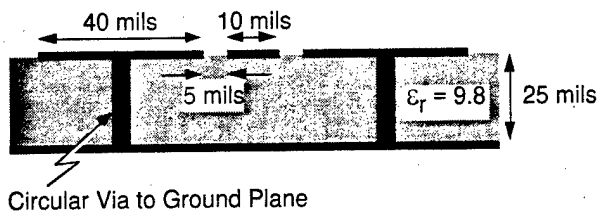


Fig. 3 Abrupt Transition from 50 Ω GCPWG to 50 Ω microstrip to 50 Ω GCPWG printed on a 25 mil Alumina Substrate. (a) Cross section of the GCPWG circuit with 50 mil spaced vias. (b) Top view of the abrupt transition (fabricated by Hughes Aircraft).

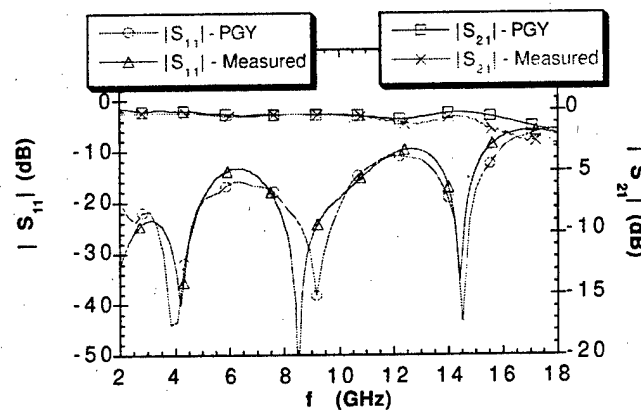


Fig. 4 Computed and Measured S-parameters for a GCPWG - microstrip transition (Measurements by Hughes Aircraft)

III Well Posed Non-Orthogonal FDTD Methods

1. Well posedness

The coupled difference equations in (1) and (2) are explicit in nature and are conditionally stable. These equations are said to be stable, providing the time step satisfies the criterion [20]:

$$\Delta t < \frac{2}{\sqrt{\lambda_{\max}(M)}} \quad (3)$$

where

$$M = C_h A_h C_e D_e A_d. \quad (4)$$

This stability condition is a necessary but not a sufficient condition to ensure the strict stability of the coupled difference equations in (1) and (2). The formulation must also be well posed [21]. If the formulation is not well posed, then it can be unconditionally unstable. The definition of well posedness will be based on the matrix M .

Definition. *The coupled system in (1) and (2) is symmetric hyperbolic if M is a Hermitian matrix. It is called strictly hyperbolic if the eigenvalues are real and distinct, strongly hyperbolic if the eigenvalues are real and there exists a complete system of eigenvectors, and weakly hyperbolic if the eigenvalues are real [21, Sect. 6.3]. The system will be ill posed if it is not at least strongly hyperbolic.*

To aide in the understanding of the above definition, it is instructive to perform an eigenvalue analysis of the coupled explicit equations. To this end, the vector

$$w^n = \begin{bmatrix} b^n \\ d^{n+\frac{1}{2}} \end{bmatrix}, \quad (5)$$

is introduced such that (1) and (2) are reposed as a first-order difference equation:

$$w^n = G w^{n-1} \quad (6)$$

where G is referred to as the growth matrix, and is more explicitly written as:

$$G = \begin{bmatrix} I & -\Delta t C_e D_e A_d \\ \Delta t C_h A_h & I - \Delta t^2 C_h A_h C_e D_e A_d \end{bmatrix}. \quad (7)$$

It can be shown that the eigenvalues of G are expressed as [20]:

$$\lambda_G = 1 - \frac{\Delta t^2 \lambda_m}{2} \pm \sqrt{\left(\frac{\Delta t^2 \lambda_m}{2}\right)^2 - 2\left(\frac{\Delta t^2 \lambda_m}{2}\right)}. \quad (8)$$

where λ_m are the eigenvalues of M . If the time step satisfies (3) and λ_m is positive real, then the term within the radical will be negative. Thus, (8) can be rewritten as

$$\lambda_G = \left(1 - \frac{\Delta t^2 \lambda_m}{2}\right) \pm j \sqrt{2\left(\frac{\Delta t^2 \lambda_m}{2}\right) - \left(\frac{\Delta t^2 \lambda_m}{2}\right)^2}. \quad (9)$$

It is seen immediately that $|\lambda_G| = 1$. This is true for all λ_m that are real and ≥ 0 providing (3) is satisfied. Interestingly, this is expected since without dissipation the total energy in the system is unchanged with time. If (3) is not satisfied, the term under the radical sign is positive, and it is immediately seen that of the two eigenvalues of G derived from (8) will be purely real and at least one of them will lie outside of the unit circle.

If the system is weakly hyperbolic, then a complete set of eigenvectors does not exist and G will be ill-conditioned which can lead to instabilities. In such a case, an eigenvalue analysis is not sufficient to determine stability. Following a pseudo spectral analysis it can be seen that an ill-conditioned system can go unstable despite its eigenvalues being on the unit circle due to the sensitivity of the system to small perturbations [22, 23].

Finally, if M has any complex eigenvalues it can easily be shown that the system will be unconditionally unstable. Specifically, assume that there exists a λ_m that is complex. Assuming that $\Delta t^2 |\lambda_m| \leq 4$, it can be shown that the eigenpair for λ_G derived from (8) has one solution inside the unit circle and the other is outside the unit circle. As an example, let $\Delta t^2 |\lambda_m| = 1 \pm j1.e - 3$, then $\lambda_G = 1.000577 \angle \pm 60^\circ$, $0.999423 \angle \pm 60^\circ$. Having a λ_G occur outside of the unit circle will lead to instability since stability requires that $|G| \leq 1$, which obviously is no longer satisfied.

The question that remains is under what practical conditions will (1) and (2) be well posed. Initially, consider the simplest case of a dual orthogonal grid that is cubic (i.e., $\Delta x = \Delta y = \Delta z$). Under such conditions, M is a real symmetric matrix. Subsequently, the system is symmetric hyperbolic, and is well posed. For a non cubic grid, M is not symmetric. Nevertheless, it is easy to show that $M = C_h C_e$ can be symmetrized through a diagonal transformation and the FDTD method is strongly hyperbolic.

Next, assume that the mesh is irregular and non-orthogonal. For sake of illustration neglect the projections A_b and A_d such that $M = C_h C_e D_e$. Interestingly, due to the complementary nature of the line integrals over the dual grid the system is strongly hyperbolic. This is true even for inhomogeneous media. Unfortunately, this formulation is only first-order accurate for general grids. Nevertheless it provides useful insight to the more general formulation.

Finally, for the most general case when the grid is irregular and non orthogonal and the projection operators are included, M is non symmetric. Because of the product of matrices, even if $C_h C_e D_e$ is symmetric, or is symmetrizable, M may not be. If the matrices A_b and A_d are non-symmetric, M will likely have complex eigenvalues. As originally proposed, the projection operators A_d and A_b derived from the NFDTD or DSI methods are non-symmetric if the grid is irregular and non orthogonal. Subsequently, both formulations can potentially suffer from late time instabilities. This is demonstrated by Roden [24].

If one can pose a technique based on the DSI/GY algorithms or NFDTD algorithms that leads to M having real and distinct eigenvalues, then the problem can be recast in a well posed manner. It is observed that if A_d and A_b are symmetric and well conditioned and ϵ_r is constant such that $D_\epsilon = \epsilon_r I$, then M will have real and distinct eigenvalues (what defines well conditionedness of A_b and A_d will be described in the next section). Interestingly, if A_d and A_b are symmetric the reaction between neighboring fields due to the projection operators are equivalent. Methods by which to derive symmetric projection matrices without sacrificing accuracy are presented in [20].

Unfortunately, if ϵ_r is inhomogeneous this may introduce complex eigenvalues in M even if A_b and A_d are symmetric. This is principally due to the non-reciprocal nature that results from the projections (e.g., $D_\epsilon A_d \neq A_d D_\epsilon$). An effective way to force symmetry in the projection operator is to approximate (6.49b) as:

$$b^n = b^{n-1} - \Delta t C_e D_\epsilon^{\frac{1}{2}} A_d D_\epsilon^{\frac{1}{2}} d^{n-\frac{1}{2}}. \quad (10)$$

Then, G is rewritten as:

$$G = \begin{bmatrix} I & -\Delta t C_e D_\epsilon^{\frac{1}{2}} A_d D_\epsilon^{\frac{1}{2}} \\ \Delta t C_h A_b & I - \Delta t^2 C_h A_b C_e D_\epsilon^{\frac{1}{2}} A_d D_\epsilon^{\frac{1}{2}} \end{bmatrix} \quad (11)$$

and

$$M \approx M_s = C_h A_b C_e D_\epsilon^{\frac{1}{2}} A_d D_\epsilon^{\frac{1}{2}}. \quad (12)$$

It can be shown that if A_d and A_b are symmetric and well conditioned, then M_s has real and distinct eigenvalues even for inhomogeneous medium.

It must be realized that M_s is an approximation. The projection operation $e = D_\epsilon^{\frac{1}{2}} A_d D_\epsilon^{\frac{1}{2}} d$ maps the normal flux density to the field intensity projected on the edge passing through the face. Examining the i -th entry of e :

$$e_i = a_{d,i,i} \frac{d_i}{\epsilon_{r_i}} + \sum_{j=1}^M a_{d,i,j} \frac{d_j}{\sqrt{\epsilon_{r_i} \epsilon_{r_j}}} \quad (13)$$

where, $a_{d,i,j}$ is the entry of matrix A_d in the i -th row and j -th column. The diagonal term of the projection operation is unchanged by the use of M_s . Whereas, the off diagonal terms are normalized by an effective permittivity expressed as the geometric mean of the permittivities of the two adjacent edges. While this is an approximation, it is demonstrated in Section 6.5.4 that this approximation does not degrade the accuracy of the NFDTD or DSI/GY algorithms.]

2. Validation

A simple example is now presented to study the accuracy of the symmetric projection operators. To this end, a benchmark test case of a circular dielectric ring in a rectangular PEC cavity is studied [25]. The geometry is provided in Fig. 5. Both unstructured and structured grids were generated to analyze this problem using the DSI and NFDTD algorithms, respectively. A cross-section of the structured and unstructured grids are illustrated in Fig. 4.

The fields in the resonant cavity were simulated using the original NFDTD algorithm and the well posed NFDTD algorithm (G^{sym}) as well as the original PGY algorithm and the well-posed algorithm PGY. The fields in the cavity were driven by injecting a vertically oriented current density placed at a non symmetric point described by:

$$\vec{J}(t) = -\hat{z} \frac{2(t-t_o)}{t_w} e^{-\frac{(t-t_o)^2}{t_w^2}}$$

where $t_w = 0.2122$ ns, and $t_o = 3t_w$. The vertical field was probed in the cavity and the time simulation was performed for 25,000 time steps with $\Delta t = 4.5$ ps. The vertical field was Fourier transformed using an FFT, and the resonant frequencies were extracted. Table 1 presents the resonant frequencies for the first 4 modes as calculated using the symmetric PGY and NFDTD methods and the measured dominant mode [25]. These results are also compared to those obtained using an implicit FETD method [6]. The results were also obtained using the non-symmetric PGY and NFDTD algorithm (G^{avg}). The resonant frequencies compared to within 0.1 % as compared to the well posed methods. It is further noted that for this case, the non-symmetric PGY method ran for 30,000 time steps before going unstable. The symmetric PGY and NFDTD methods ran for 250,000 time steps and still showed no signs of instability.

The dielectric ring in cavity problem was repeated when the dielectric relative permittivity was increased to 9.8. For this case, the grid density in and near the ring was roughly doubled to properly resolve the fields. The calculated resonant frequencies are presented in Table 2. Again, the symmetric DSI/GY simulation was stable for over 250,000 time steps. Interestingly, the symmetric NFDTD simulation did eventually go unstable in the very late time for this geometry. Observing the refined NFDTD lattice, it was observed that there were four cells with highly obtuse interior angles. This lead to an ill-conditioned matrix as discussed in the previous section. This is a penalty of structured gridding.

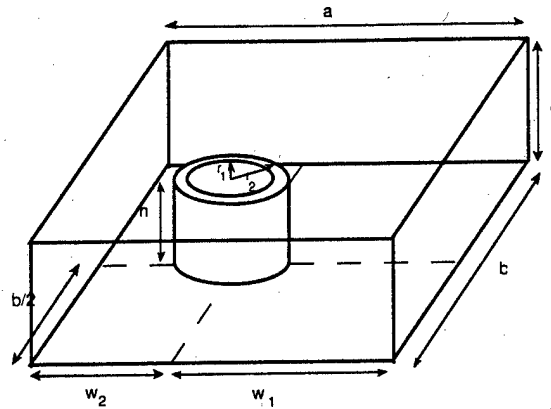


Fig. 5 Dielectric ring in a rectangular PEC cavity ($a = 324$ mm, $b = 121$ mm, $c = 43$ mm. The ring is centered at $w_1 = 207.25$ mm, $w_2 = 116.75$ mm, $b/2$ along the y -direction and rests on the ground plane. The ring has a height of $h = 39$ mm, inner radius $r_1 = 16.65$ mm, and outer radius $r_2 = 26.75$ mm.)

Table 1
Resonant Frequencies of the Dielectric Ring Loaded Cavity, $\epsilon_r = 2.06$

Mode	Meas.	WP-DSI	G^{sym}	FETD
k01	1.258 GHz	1.258 GHz	1.258 GHz	1.259 GHz
k02	-	1.509 GHz	1.509 GHz	1.512 GHz
k03	-	1.836 GHz	1.835 GHz	1.841 GHz
k04	-	2.158 GHz	2.161 GHz	2.175 GHz

Table 2
Resonant Frequencies of the Dielectric Ring Loaded Cavity, $\epsilon_r = 9.8$

Mode	WP-DSI	G^{sym}	FETD
k01	0.9520 GHz	0.9520 GHz	0.9518 GHz
k02	1.415 GHz	1.415 GHz	1.420 GHz
k03	1.608 GHz	1.612 GHz	1.615 GHz
k04	2.024 GHz	2.026 GHz	2.034 GHz

IV Uniaxial Perfectly Matched Layer Truncation of Computational Space for Simulation of Unbounded Domains.

1. Introduction

Explicit time-domain methods such as the finite-difference time-domain (FDTD) method and the planar generalized Yee (PGY) algorithm have been highly effective for the analysis of practical microwave circuit devices and antennas. One of the most challenging aspects of these methods is implementing absorbing boundary conditions that can accurately truncate the mesh over broad frequency bands. The perfectly matched layer (PML) absorbing media introduced by J.-P. Berenger [26] has been demonstrated to be a highly effective method for the termination of FDTD lattices [27, 28]. and can result in reflection errors as minute as -80 dB to -100 dB. Recently, it has been shown that the PML method can be reposed in a Maxwellian form as a uniaxial anisotropic medium [14, 15, 29]. It has been demonstrated that the uniaxial medium can be perfectly matched to lossy, inhomogeneous, dispersive, isotropic and anisotropic medium. Most significant is that the extension to such complex media in a FDTD implementation is quite trivial. Furthermore, since the uniaxial PML formulation is Maxwellian and not restricted to an orthogonal field splitting and it can be easily extended to more generalized methods such as the non-orthogonal FDTD method [16]. The focus of this summary will be on the efficient implementation of the uniaxial PML method and the expected accuracy. The simple extension to more complex media will also be discussed in the context that its implementation within an existing FDTD code is quite trivial.

2. The Uniaxial PML

It was shown in [14, 15, 29] that an arbitrary polarized wave incident on a planar half space (defined by the $z = 0$ plane) will be perfectly transmitted provided that the half space is a uniaxial medium with constitutive parameters

$$\bar{\bar{\epsilon}} = \epsilon_o \epsilon_r \begin{bmatrix} s_z & 0 & 0 \\ 0 & s_z & 0 \\ 0 & 0 & s_z^{-1} \end{bmatrix}, \quad \bar{\bar{\mu}} = \mu_o \mu_r \begin{bmatrix} s_z & 0 & 0 \\ 0 & s_z & 0 \\ 0 & 0 & s_z^{-1} \end{bmatrix} \quad (14)$$

where ϵ_r and μ_r are defined by the medium of the upper half space. It can be demonstrated that this perfectly transmitting property is still valid if the upper half space is inhomogeneous, lossy, dispersive, and even anisotropic.

The intention of the PML medium is to rapidly attenuate waves entrant into the medium. Thus a suitable choice for s_z is:

$$s_z = \kappa_z + \frac{\sigma_z}{j\omega\epsilon_o}. \quad (15)$$

Given the propagation constant of the incident wave to be $\gamma_z^i = \alpha_z^i + j\beta_z^i$, then it can be shown that the propagation constant of the transmitted wave in the uniaxial PML region is [15]

$$\gamma_z^a = \left(\kappa_z \alpha_z^i + \beta_z^i \frac{\sigma_z}{\omega \epsilon_0} \right) + j \left(\kappa_z \beta_z^i - \alpha_z^i \frac{\sigma_z}{\omega \epsilon_0} \right). \quad (16)$$

The real part of γ_z^a leads to the attenuation of the wave. Thus, the loss term σ_z will lead to the attenuation of all propagating modes, and the real term κ_z will lead to the amplification of the attenuation of all evanescent modes incident on the planar interface. As a result, this parameterization is analogous to the generalized PML introduced by Fang *et al.* [30], which is an extension of the original Berenger formulation.

The uniaxial PML can be used to terminate a three-dimensional FDTD space accurately and efficiently. To this end, the FDTD lattice is terminated on all 6 sides via planar PML media, which are backed by a PEC wall. Under such circumstances, it is recognized that the planar interfaces will overlap in what is referred to as the corner regions. In order to derive the constitutive relations in these corner regions, it is reasonable to match the PML to the adjacent uniaxial medium. For example, let the upper half space have permittivity and permeability tensors:

$$\bar{\epsilon}_1 = \epsilon_0 \epsilon_r \begin{bmatrix} s_x^{-1} & 0 & 0 \\ 0 & s_x & 0 \\ 0 & 0 & s_x \end{bmatrix}, \quad \bar{\mu}_1 = \mu_0 \mu_r \begin{bmatrix} s_x^{-1} & 0 & 0 \\ 0 & s_x & 0 \\ 0 & 0 & s_x \end{bmatrix}. \quad (17)$$

Then, assuming an arbitrary polarized plane wave will be perfectly transmitted into the lower half space separated by a $z = \text{constant}$ plane if the permittivity and permeability tensors are defined as:

$$\bar{\epsilon}_2 = \epsilon_0 \epsilon_r \begin{bmatrix} s_x^{-1} & 0 & 0 \\ 0 & s_x & 0 \\ 0 & 0 & s_x \end{bmatrix} \begin{bmatrix} s_z & 0 & 0 \\ 0 & s_z & 0 \\ 0 & 0 & s_z^{-1} \end{bmatrix}, \quad \bar{\mu}_2 = \mu_0 \mu_r \begin{bmatrix} s_x^{-1} & 0 & 0 \\ 0 & s_x & 0 \\ 0 & 0 & s_x \end{bmatrix} \begin{bmatrix} s_z & 0 & 0 \\ 0 & s_z & 0 \\ 0 & 0 & s_z^{-1} \end{bmatrix}. \quad (18)$$

This can be further generalized to a y interface, leading to the general anisotropic tensors

$$\bar{\epsilon} = \epsilon_0 \epsilon_r \bar{s}, \quad \bar{\mu} = \mu_0 \mu_r \bar{s}, \quad \text{and} \quad \bar{s} = \begin{bmatrix} \frac{s_x s_z}{s_x} & 0 & 0 \\ 0 & \frac{s_x s_z}{s_y} & 0 \\ 0 & 0 & \frac{s_x s_y}{s_z} \end{bmatrix} \quad (19)$$

where,

$$s_x = \left(\kappa_x + \frac{\sigma_x}{j\omega \epsilon_0} \right), \quad s_y = \left(\kappa_y + \frac{\sigma_y}{j\omega \epsilon_0} \right), \quad s_z = \left(\kappa_z + \frac{\sigma_z}{j\omega \epsilon_0} \right). \quad (20)$$

Within this uniaxial region, Maxwell's curl equations are expressed as:

$$\nabla \times \bar{H} = j\omega \epsilon_0 \epsilon_r (\omega) \bar{s} \bar{E}, \quad \nabla \times \bar{E} = -j\omega \mu_0 \bar{s} \bar{H} \quad (21)$$

It is from these equations that the explicit field updates will be derived. As an example, consider the update expression for E_z . Introducing the constitutive relation

$$D_z = \varepsilon_o \varepsilon_r \frac{s_x}{s_z} E_z. \quad (22)$$

where ε_r is assumed to be a function of x and y , it follows from (6) - (8):

$$\frac{\partial}{\partial x} H_y - \frac{\partial}{\partial y} H_x = j\omega D_z + \frac{\sigma_y}{\varepsilon_o} D_z. \quad (23)$$

Subsequently, this leads to the discrete field update for D_z :

$$D_z^{n+\frac{1}{2}} = \frac{\frac{\kappa_y}{\Delta t} - \frac{\sigma_y}{2\varepsilon_o}}{\frac{\kappa_y}{\Delta t} + \frac{\sigma_y}{2\varepsilon_o}} D_z^{n-\frac{1}{2}} + \frac{1}{\frac{\kappa_y}{\Delta t} + \frac{\sigma_y}{2\varepsilon_o}} \left(\left(H_y^n_{i+\frac{1}{2},j,k+\frac{1}{2}} - H_y^n_{i-\frac{1}{2},j,k+\frac{1}{2}} \right) / \Delta x - \left(H_x^n_{i,j+\frac{1}{2},k+\frac{1}{2}} - H_x^n_{i,j-\frac{1}{2},k+\frac{1}{2}} \right) / \Delta y \right) \quad (24)$$

Given D_z , an auxiliary relationship can be derived for E_z as

$$s_z D_z = \varepsilon_o \varepsilon_r s_x E_z, \text{ or} \quad (25)$$

$$j\omega \kappa_z D_z + \frac{\sigma_z}{\varepsilon_o} D_z = \varepsilon_o \varepsilon_r (j\omega \kappa_x E_z + \frac{\sigma_x}{\varepsilon_o} E_z).$$

Then, transforming (25) into the time-domain, approximating the time derivatives using a central difference approximation, and averaging $\frac{\sigma_z}{\varepsilon_o} D_z$ and $\frac{\sigma_x}{\varepsilon_o} E_z$ in time, this results in a second-order accurate explicit update equation:

$$E_z^{n+\frac{1}{2}} = E_z^{n-\frac{1}{2}} \frac{(\kappa_x - \frac{\sigma_x \Delta t}{2\varepsilon_o})}{(\kappa_x + \frac{\sigma_x \Delta t}{2\varepsilon_o})} + \frac{1}{(\kappa_x + \frac{\sigma_x \Delta t}{2\varepsilon_o}) \varepsilon_o \varepsilon_r} \left(D_z^{n+\frac{1}{2}} (\kappa_z + \frac{\sigma_z \Delta t}{2\varepsilon_o}) - D_z^{n-\frac{1}{2}} (\kappa_z - \frac{\sigma_z \Delta t}{2\varepsilon_o}) \right). \quad (26)$$

Similar update equations can be derived for the remaining field components.

The uniaxial PML method is easily extended to more general media such as lossy media, dispersive media, or non-linear media. This can easily be done through the addition of an additional auxiliary equation(s) [15], which is a simple extension of the above algorithm.

3. Matching PML to Generalized Media

In the previous section, the PML was matched to a homogeneous medium supporting plane wave type solutions impinging on the PML boundary. Because the PML is matched for all angles of incidence and polarizations, one could generalize this to arbitrary finite sources, or scattered fields emanating from complex geometries by using plane wave expansions of the fields. However, a more general proof is needed to demonstrate its effectiveness for matching to waves propagating in inhomogeneous media. This is the focus of this section.

Consider a wave propagating in an inhomogeneous media along an axial direction, chosen arbitrarily to be the z -axis. It is assumed that the material medium is inhomogeneous along the transverse axes (x,y) , and invariant along the axial direction. The electromagnetic waves

supported by such a medium can be decomposed into TE_z and TM_z polarized waves. In this medium, we pose time-harmonic solutions to the wave equation of the form:

$$TE_z: \quad H_z = h_z(x, y)e^{-\gamma_z z}, \quad (27)$$

$$TM_z: \quad E_z = e_z(x, y)e^{-\gamma_z z}, \quad (28)$$

where, $E_z = 0$ for the TE_z polarized waves, and $H_z = 0$ for the TM_z polarized waves. From Maxwell's equations, the remaining fields can be derived from the axial fields as:

$$\begin{aligned} E_x &= \frac{-j\omega\mu}{k^2 + \gamma_z^2} \frac{\partial H_z}{\partial y}, & H_x &= \frac{-\gamma_z}{k^2 + \gamma_z^2} \frac{\partial H_z}{\partial x}, \\ E_y &= \frac{j\omega\mu}{k^2 + \gamma_z^2} \frac{\partial H_z}{\partial x}, & H_y &= \frac{-\gamma_z}{k^2 + \gamma_z^2} \frac{\partial H_z}{\partial y}, \\ E_z &= 0, \end{aligned} \quad (29)$$

for the TE_z polarization. The TM_z fields are derived from (28) leading to a dual expression of (29).

A PML half space is interfaced with the inhomogeneous medium in the $z = 0$ plane. It is assumed that the transversely inhomogeneous material profile extends through the PML. From (19), the PML has the constitutive relations related to the z -normal interface:

$$\bar{\bar{\epsilon}} = \epsilon(x, y) \begin{bmatrix} s_z & 0 & 0 \\ 0 & s_z & 0 \\ 0 & 0 & s_z^{-1} \end{bmatrix}, \quad \bar{\bar{\mu}} = \mu(x, y) \begin{bmatrix} s_z & 0 & 0 \\ 0 & s_z & 0 \\ 0 & 0 & s_z^{-1} \end{bmatrix}$$

where ϵ and μ can be complex. The generalized wave equation is then derived, and the axial field solutions are then derived for the dual polarizations:

$$TE_z: \quad H_z = s_z h_z(x, y)e^{-s_z \gamma_z z}, \quad (30)$$

$$TM_z: \quad E_z = s_z e_z(x, y)e^{-s_z \gamma_z z}, \quad (31)$$

where, $h_z(x, y)$ and $e_z(x, y)$ are identical to those in (27) and (28), respectively. Note that the s_z weighting the normal fields is consistent with Gauss' laws. For the TE_z polarized case, the remaining fields are again derived from Maxwell's equations in the uniaxial medium, leading to:

$$\begin{aligned} E_x &= \frac{-j\omega\mu}{k^2 + \gamma_z^2} \frac{1}{s_z} \frac{\partial H_z}{\partial y}, & H_x &= \frac{-\gamma_z}{k^2 + \gamma_z^2} \frac{1}{s_z} \frac{\partial H_z}{\partial x}, \\ E_y &= \frac{j\omega\mu}{k^2 + \gamma_z^2} \frac{1}{s_z} \frac{\partial H_z}{\partial x}, & H_y &= \frac{-\gamma_z}{k^2 + \gamma_z^2} \frac{1}{s_z} \frac{\partial H_z}{\partial y}, \\ E_z &= 0, \end{aligned} \quad (32)$$

The TM_z fields are simply the dual of (32).

Finally, it is seen that inserting the axial fields in (30) in (32), and (27) in (29), the transverse fields are continuous across the $z = 0$ plane. Furthermore, it is seen that the wave transmitted into the PML medium has the same characteristic wave impedance relative to the axial direction as that

of the impinging waves for both polarizations. Subsequently, the proposed uniaxial medium is perfectly matched to the inhomogeneous space.

4. Reflection Error

The preceding theoretical analyses have assumed the PML to be a half space. Employing the PML to truncate the FDTD lattice boundaries, the PML have a finite thickness and terminated by a boundary. If the exterior boundary is assumed to be a perfectly electrical conducting (PEC) wall, there will be reflected power back into the interior FDTD region. The reflection can be calculated using a simple transmission line analysis and will have an amplitude of:

$$R(\theta) = e^{-2\sigma\eta\epsilon_r d \cos\theta} \quad (33)$$

where θ is the angle of incidence, d is the thickness of the PML slab, η is the characteristic impedance of the reference material, and σ is the conductivity of the PML. Within the context of an FDTD simulation $R(\theta)$ is referred to as the "reflection error" since it is a non-physical reflection due to the PEC backed PML slab. This reflection error decays exponentially with the thickness of the PML as well as with the conductivity of the PML. However, the cosine dependence of θ dictates that at higher angles of incidence, the reflection error will increase for a fixed σ and d . To be effective within an FDTD simulation, it is desirable for the PML medium to be as thin as possible. Thus, for a small d , one must have a large conductivity to reduce $R(\theta)$ to an acceptably small level.

The PML interface presents a discontinuity in both the electrical and magnetic conductivity. In the discrete space representation of Maxwell's curl equations via the FDTD method, it is realized that these discontinuities are modeled using a linear approximation [31]. Furthermore, σ and σ^* are staggered by one half of a lattice cell due to a staggering of the electric and magnetic fields. Subsequently, large discontinuities in σ and σ^* will lead to significant discretization error which will manifest as a spurious reflection. To reduce this reflection error, it was proposed by Berenger to spatially scale the conductivity profile along the normal axis [26]. It can be shown that as long as the conductivity is scaled along the normal axes, then the material is still perfectly matched.

In the continuous space, assume that σ is a function of x . Assuming a PEC backed PML slab of thickness d , the reflection due to a purely propagating wave impinging at angle θ is:

$$R(\theta) = e^{-2\eta\epsilon_r \cos\theta \int_0^d \sigma(x) dx} \quad (34)$$

A few profiles have been suggested for scaling σ . The most successful have been a polynomial scaling and a geometric scaling [32]. The polynomial scaling is simply:

$$\sigma(x) = \left(\frac{x}{d}\right)^m \sigma_{\max} \quad (35)$$

This scales the conductivity from 0 at the PML – working volume (WV) interface to σ_{\max} at the PEC boundary. The resultant reflection coefficient is:

$$R(\theta) = e^{-2\eta\epsilon_r\sigma_{\max}d\cos\theta/(m+1)} \quad (36)$$

Polynomial scaling provides two parametric coefficients for a fixed PML thickness: σ_{\max} and m . The larger m , the flatter the conductivity will be near the PML – WV interface. Deeper into the PML, the conductivity increases more rapidly. In this region, the field amplitudes have decayed substantially and the reflections due to discretization error contribute less. Typically m in the range between 3 and 4 has been found to be suitable [14, 32-34].

If the real part of s is > 1 , then it can also be spatially scaled using the polynomial scaling. Thus, κ will scale from 1 to some maximum value κ_{\max} at the PEC boundary. To this end:

$$\kappa(x) = 1 + (\kappa_{\max} - 1) \left(\frac{x}{d} \right)^m \quad (37)$$

where $\kappa_{\max} \geq 1$.

For polynomial scaling, the parameters can be determined for a given error estimate. For example, given m and d , it is desired to achieve a reflection error of $R(0)$, then from (7.60) σ_{\max} is computed as:

$$\sigma_{\max} = -\frac{\ln(R(0))(m+1)}{2\eta\epsilon_r d} \quad (38)$$

Geometric scaling scales the conductivity profile geometrically. Let Δx be the spatial increment of the FDTD lattice. Then [33],

$$\sigma(x) = \left(g^{\frac{1}{\Delta x}} \right)^x \sigma_o \quad (39)$$

Specifically, the conductivity scales from σ_o at the PML – WV interface to $g^N \sigma_o$ at the PEC boundary, where $d = N\Delta x$ is the thickness of the PML slab. From (7.58), this results in a reflection coefficient of:

$$R(\theta) = e^{-2\eta\sigma_o\Delta x(g^N - 1)\cos\theta/\ln g} \quad (40)$$

For geometric scaling, there are two parameters to choose for a fixed d : g and σ_o . σ_o is the conductivity in the $x = 0$ plane, or the PML/WV interface. Thus, it must be small to minimize the initial discretization error. The metric g governs the rate of increase of the conductivity deeper into the medium. Of course, g is always greater than 1. The larger g , the flatter the conductivity profile near the interface, and the steeper it increases deeper into the PML slab.

Again, if κ is > 1 , then it can also be geometrically scaled as:

$$\kappa(x) = \left(q^{\frac{1}{\Delta x}} \right)^x \quad (41)$$

Thus, κ will scale from 1 to some maximum value q^N at the PEC boundary.

For geometric scaling, one would predetermine g , d , and $R(0)$. Then,

$$\sigma_o = -\frac{\ln(R(0))\ln(g)}{2\eta\epsilon_r\Delta x(g^N - 1)} \quad (42)$$

where $d = N\Delta x$ is the thickness of the PEC backed PML layer.

The design of the optimal PML results in a delicate balance of the theoretical reflection error $R(\theta)$ and discretization error. For example, (38) provides σ_{\max} for a spatially scaled conductivity given a predetermined $R(\theta)$ and m . In practice, if σ_{\max} is small, the predominant reflection of the finite PML will be due to PEC backed wall. In fact, (36) provides a fairly accurate approximation of the reflection error if σ_{\max} is sufficiently small. However, in practice one would rather choose σ_{\max} to be as large as possible to minimize $R(\theta)$. Unfortunately, if σ_{\max} is too large, then discretization error due to the FDTD approximation will dominate and the actual reflection error will be orders of magnitude higher than what (36) predicts. Subsequently, there is an optimal choice for $R(\theta)$ which balances reflection from the PEC wall and discretization error.

It was postulated by Berenger in [32, 33] that the largest discretization error manifesting as reflection error occurs at the PML interface. Energy that penetrates into the PML that is subsequently reflected will be attenuated before exiting the PML and typically is not as large a contribution. Thus, it is desirable to minimize the step discontinuity at the PML interface. One way to achieve this is by spatially scaling the conductivity in the PML as presented earlier in this section. In fact, for larger m or larger g , the flatter the conductivity profile near $x = 0$, thus reducing $\sigma_x(0)$. However, if m or g become too large, then reflections from deeper within the PML will begin to dominate.

For geometric scaling, the optimal g is typically between 2 and 3. For polynomial scaling, the optimal m is typically between 3 and 4. Through extensive experimental study, it was demonstrated in [14, 35] that for a broad range of applications an optimal choice for a 10 cell thick PML is safely assumed to be $R(0) \approx e^{-16}$. For a 5 cell thick PML, $R(0) \approx e^{-8}$ is optimal. From (38), this leads to an optimal choice for σ_{\max} :

$$\sigma_{\text{opt}} = \frac{(m+1)}{150\pi\sqrt{\epsilon_r}\Delta x} \quad (43)$$

where Δx is the grid spacing along the axial direction. For many cases, σ_{opt} will be close to minimizing the reflection error, and this value has proven to be quite robust and applicable for many applications, as will be further illustrated below.

5. Validation

To demonstrate the effectiveness of the PML, consider a current source radiating in an unbounded medium, as illustrated in Fig. 6. The source is a vertically directed current source that is invariant along the axial z -direction. Hence, it will radiate two-dimensional TE_z waves.

A two-dimensional adaptation of the FDTD algorithm truncated by UPML media was implemented. The FDTD lattice used to simulate this problem consisted of a 40 mm x 40mm region. The spatial discretization used assumed $\Delta x = \Delta y = 1$ mm, and the time step was 0.98 of the Courant limit ($\Delta t = 0.92457$ ps). Hence a 40 x 40 cell lattice was employed in the working volume region. The vertical current source was placed in the center of the computational domain and had a differentiated Gaussian pulse time signature:

$$J_y(x_o, y_o, t) = -2 \frac{t - t_o}{t_w} e^{-\left(\frac{t - t_o}{t_w}\right)^2} \quad (44)$$

where the pulse half width $t_w = 2.65258 \times 10^{-11}$ s, and the pulse delay $t_o = 4 t_w$. Note that the amplitude is scaled by t_w . The electric field was probed at two points, *A* and *B*, as illustrated in Fig. 6. *A* is in the same plane as the source and two cells from the PML interface, and *B* is two cells from the bottom and side PML walls. The electromagnetic fields were simulated over 1000 time steps, which is well past the steady state response.

Both a 5 and 10 cell uniaxial PML absorbing medium was used to terminate each exterior boundary. The PML parameters were scaled using a polynomial scaling, where $m = 4$, $\sigma_{\max} = \sigma_{\text{opt}}$, and $\kappa_{\max} = 1$. The relative error computed at points *A* and *B* due to 5 and 10 cell thick PML layers as a function of time is illustrated in Fig. 7. To compute the relative error at points *A* and *B*, a reference simulation was performed a priori using a 1240 x 1240 cell lattice with the current source located at the center of the lattice and the fields at points *A* and *B* at the same relative positions. The grid was made sufficiently large such that no reflections from any boundaries would be present in the reference solution. It is noted that the error is related to the maximum field value at that point during the time simulation.

Observing Fig. 7, it is seen that the maximum error occurs in late time. This error is predominately low frequency error as anticipated. As time advances further, this error gradually decreases. It is also observed that the error at point *A* is always less than that at point *B*. This is mainly because the wave impinging on the wall near point *A* is predominately normally incident. Thus, maximum absorption is seen. At point *B*, the amplitude of the wave is smaller, due to the radiation pattern of the source, and the wave impinges on the boundaries at 45°.

The relative error in Fig. 7 was computed assuming a fixed $\sigma_{\max} (= \sigma_{\text{opt}})$. Additional information can be gained by observing the maximum error over 1,000 time iterations recorded at points *A* and *B* as a function of σ_{\max} . This is illustrated in Fig. 8, where σ_{\max} is varied from 0 to 3 times σ_{opt} for the 5 and 10 cell thick PML layers. It is noted that the same σ_{\max} was used for each of the four boundaries, and $m = 4$ was again assumed. Interestingly, at points *A* and *B*, the optimal choice for σ_{\max} is quite close to σ_{opt} . Again, though, the maximum error in the fields at point *B* is roughly an order of magnitude larger than the error at point *A* for 5 and 10 cells thick

PMLs. Fig. 9 illustrates the error for a 15 cell PML, and it is shown that for $\sigma_{\max} = \sigma_{\text{opt}}$, that the errors at both points *A* and *B* are the same, and more than 5 digits of accuracy are realized.

A more comprehensive study of the reflection error is offered by Fig. 10. Specifically, Figs. 10.a and 10.b are contour plots of the maximum relative error at points *A* and *B*, respectively, recorded over 1000 time iterations versus the conductivity σ_{\max} normalized by σ_{opt} as well as the polynomial order m . It is noted that m is not necessarily an integer, and was scaled from 1 to 5. It is observed that the minimum error is found for when m is between 3 and 4, and when σ_{\max} is roughly 75 % of σ_{opt} . Even if σ_{opt} is chosen, the reflection error on the order of -90 dB at point *A* and -75 dB at point *B*.

A similar study is performed when geometric scaling is used to scale the PML parameters. Figure 11 is a contour plot of the maximum relative error over 1000 time steps at points *A* and *B* versus $R(0)$ and g for a 10 cell thick PML. Interestingly, for $g = 2.2$, roughly -85 dB of reflection error is realized at both points *A* and *B* when $\ln(R(0))$ is between -12 and -16. It is also observed that the effectiveness of the PML is quite sensitive to the choice of g .

As a final example, consider a printed antenna analyzed using the FDTD and the uniaxial PML boundary condition. The geometry of the patch antenna that was simulated is superimposed in the graph in Fig. 12. This antenna was previously analyzed in [36, 37]. The discretization used for this problem was $\Delta x = 0.389$ mm, $\Delta y = 0.4$ mm, $\Delta z = 0.1588$ mm, and $\Delta t = 0.441$ ps. The source microstrip line was 50 cells long and was excited by a voltage source with a Gaussian profile and a 30 GHz bandwidth. The interfaces of the PML media were placed 3 cells from the edge of the patch antenna, and 5 cells above the surface of the antenna. The PML slabs were 10 cells thick. A spatial scaling with $m = 4$, and σ_{opt} from (7.67) were used. Fig. 7.25 compares the reflection loss $|S_{11}|$ computed using the FDTD and the PML boundary that was positioned as described above, with the case when the PML boundaries were placed much further away. Negligible difference is observed in the result over most of the frequency band. However, as expected, there is some small error at very low frequency.

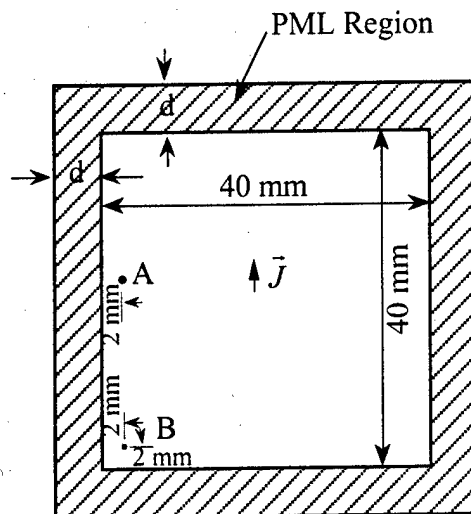


Fig. 6 TE-polarized wave excited by a vertically directed electric current source in a two-dimensional region. The working volume is 40 mm x 40mm, and is surrounded by PML layers of thickness d . The source is located at the center of the region. The fields are probed at two observation points A and B.

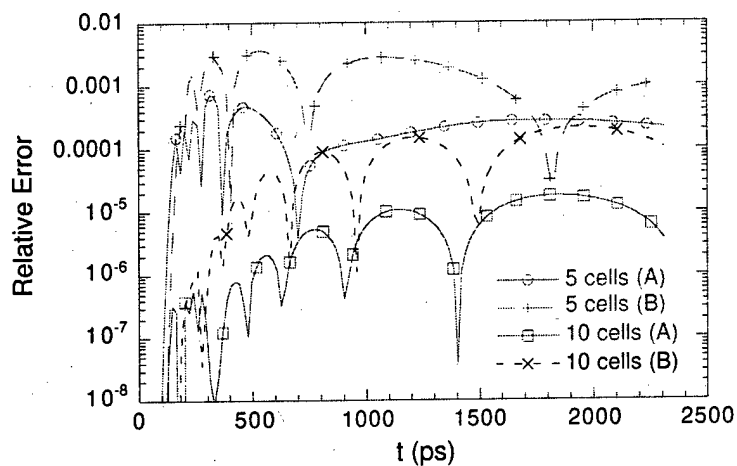


Fig. 7 Relative error at points A and B over 1,000 time iterations for 5 and 10 cell thick PMLs terminating a 40 x 40 cell lattice excited by a small dipole with $\sigma_{\max} = \sigma_{\text{opt}}$ and $\kappa = 1$.

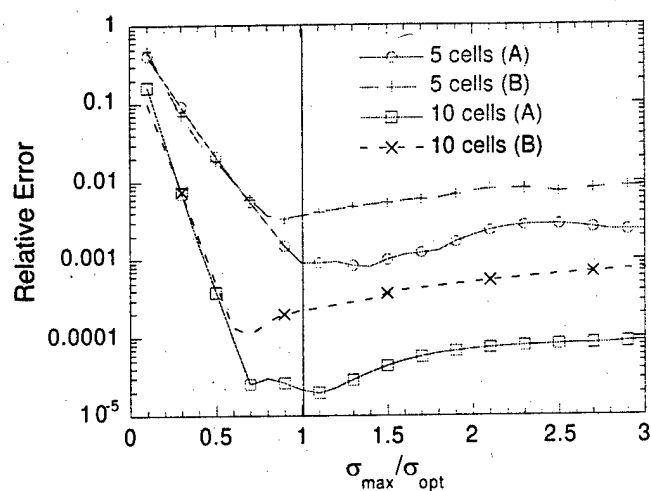


Fig. 8 Maximum relative error due to a 5 and 10 cell thick PML termination of a 40×40 cell lattice excited by a small dipole over 1,000 time iterations versus $\sigma_{\max}/\sigma_{\text{opt}}$ ((7.67)). Polynomial spatial scaling with $m = 4$ and $\kappa = 1$.

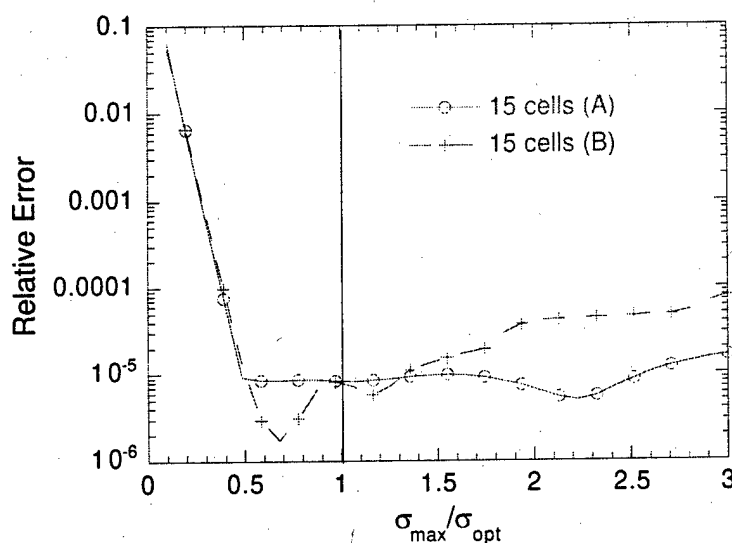


Fig. 9 Maximum relative error due to a 15 thick PML termination of a 40×40 cell lattice excited by a small dipole over 1,000 time iterations versus $\sigma_{\max}/\sigma_{\text{opt}}$ ((7.67)). Polynomial spatial scaling with $m = 4$ and $\kappa = 1$.

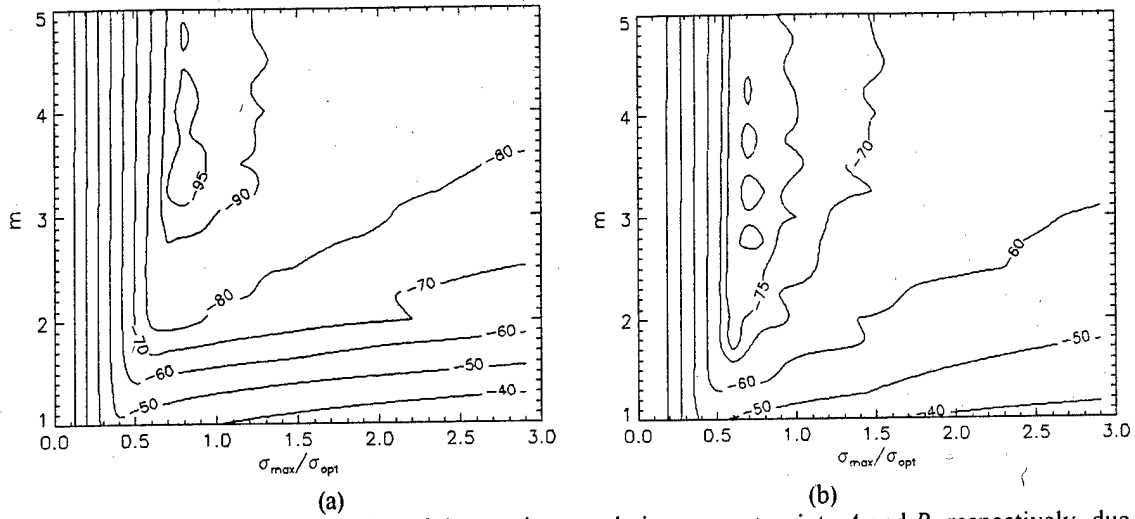


Fig. 10 Contour plot of the maximum relative error at points *A* and *B*, respectively, due to a polynomial scaled 10 cell thick PML termination of a 40 x 40 cell lattice excited by a small dipole over 1,000 time iterations versus $\sigma_{\max}/\sigma_{\text{opt}}$ and m .

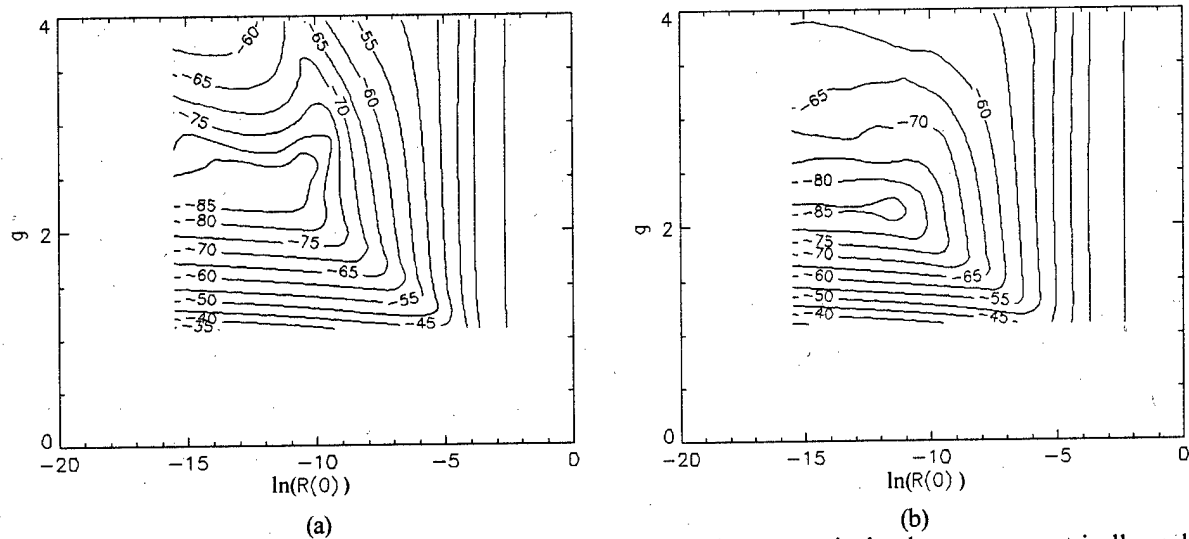


Fig. 11 Maximum relative error at points *A* and *B*, respectively, due to a geometrically scaled 10 cell thick PML termination of a 40 x 40 cell lattice excited by a small dipole over 1,000 time iterations versus g and $\ln(R(0))$.

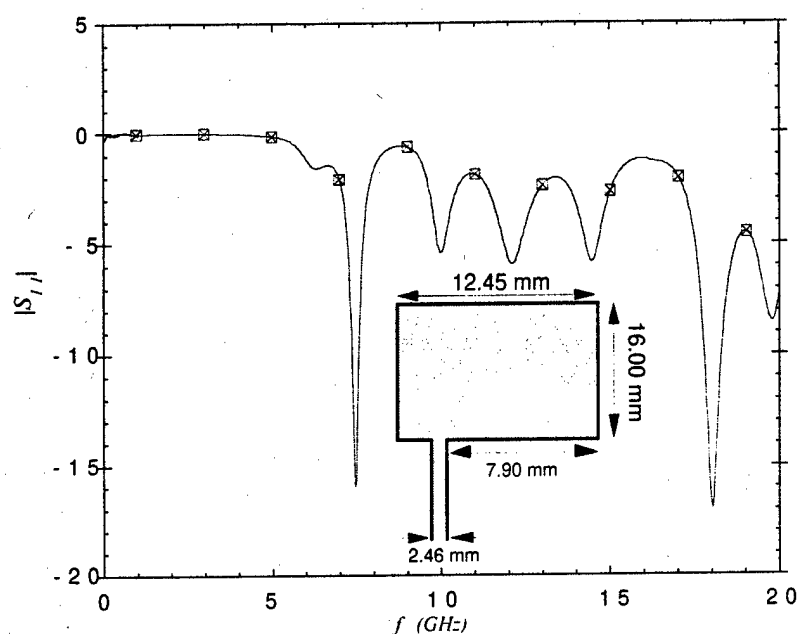


Fig. 12 $|S_{11}|$ of a microstrip fed patch antenna (superimposed) printed on a 31.25 mil Duroid substrate ($\epsilon_r = 2.2$) computed via the FDTD method. The FDTD lattice is terminated by a 10-cell thick uniaxial PML layer which is placed: — \times — 3 cells from the edge of the patch and 5 cells above the patch, and — \square — 10 cells from the edges of the patch. Source: Gedney, *IEEE Transactions on Antennas and Propagation*, vol. 44, pp. 1630-1639, December 1996.

V Parallel Finite-Element Frequency-Domain Method

1. Introduction

The finite element method (FEM) is an effective means for analyzing a plethora of electromagnetic problems. The FEM's principal attribute is that it efficiently models highly irregular geometries as well as penetrable and inhomogeneous material media. Secondly, the linear system of equations that results from a FEM discretization is highly sparse and can be solved using efficient solution techniques for sparse matrices. The focus of this section is on the development of an efficient parallel algorithm for the solution of the sparse matrix arising from an FEM formulation. An early approach to this problem was a divide-and-conquer technique developed by Patterson *et al.* [38, 39]. This approach consisted of partitioning the global matrix using an automatic partitioning scheme. Subsequently, a global iterative solver based on the Bi Conjugate Gradient (BiCG) method was used to solve the distributed sparse matrix.

Alternatively, a parallel direct solution method for two-dimensional FEM analysis was introduced by Lee and Chupongstimun [40]. This technique coupled the subdomain solutions by enforcing tangential field continuity between adjacent subdomains leading to a global matrix representing only the tangential fields on the shared boundaries. The global matrix is much smaller than the original FEM matrix and can be solved using a direct method.

In [41], Deprés introduced a hybrid iterative DMM for the two-dimensional Helmholtz problem. To this end, an iterative method was proposed, for which each iteration consists of solving the fields interior to each subdomain and then constraining the field continuity at the interface of each subdomain by enforcing a Robin-type transmission condition on the boundary fields (this transmission condition essentially enforces the continuity of both the tangential electric and magnetic field intensities across the shared boundaries). Deprés also introduced a relaxation scheme in [42] which greatly accelerated the iterative process. Later Stupfel [43] extended this method by prescribing a new ABC [44] at the exterior boundary and using an "onion like" partition of the computational domain improving the efficiency of the transmission condition and overall performance of this DDM.

The focus of this research is on the application of a hybrid iterative solution based on the method of Lagrange multipliers. This method is modeled after Finite Element and Tearing Interconnecting (FETI) method originally developed by Farhat and Roux [45]. Specifically, the FEM discretization of the weak form equation for each subdomain will be posed. The solutions of each subdomain will be constrained through the use of Lagrange multipliers by enforcing the continuity of the tangential fields across each boundary interface. A reduced system of equations representing the Lagrange multipliers is then derived and is solved using a Conjugate Gradient (CG) algorithm. The advantage of this method is that each subregion can be solved completely independently,

lending to a scalable algorithm. Secondly, the number of iterations required to solve the global problem is dependent on the order of the matrix representing the Lagrange multipliers as opposed to the global matrix.

2. Formulation

Assume that a lossy inhomogeneous half space is interfaced with a uniaxial anisotropic medium in the $z = 0$ plane. In the anisotropic medium, Maxwell's equations are described in the frequency domain as

$$\nabla \times \vec{E} = -j\omega\mu_0\mu_r\vec{s}\vec{H}, \quad \nabla \times \vec{H} = j\omega\epsilon_0\hat{\epsilon}_r\vec{s}\vec{E} \quad (45)$$

where $\hat{\epsilon}_r$ is complex and frequency dependent, and \vec{s} is the tensor in equation (19).

The vector wave equation in the uniaxial medium is then derived from (45):

$$\nabla \times \mu_r\vec{s}^{-1} \nabla \times \vec{E} - \omega^2\mu_0\epsilon_0\hat{\epsilon}_r\vec{s}\vec{E} = 0 \quad (46)$$

where UPML is assumed throughout the volume. Performing the inner product with a testing function defined over the finite volume Ω , and utilizing Green's first identity results in the weak form equation:

$$\iiint_{\Omega} \left[\nabla \times \vec{T} \cdot \mu_r\vec{s}^{-1} \nabla \times \vec{E} - \omega^2\mu_0\epsilon_0\hat{\epsilon}_r\vec{T} \cdot \vec{s}\vec{E} \right] d\Omega - \iint_{\partial\Omega} \left[\vec{T} \cdot \hat{n} \times \mu_r\vec{s}^{-1} \nabla \times \vec{E} \right] dA = 0 \quad (47)$$

The finite element solution is performed by discretizing the volume into element domains, and expanding the testing and trial vector functions using vector edge elements (in this paper first-order Whitney elements are employed). Then, the first variation of (47) is evaluated at the stationary point, leading to a sparse linear system of equations.

Inside the working volume, the medium is assumed to be isotropic. Specifically from (19) and (20), \vec{s} reduces to the identity tensor. Within the PML region, \vec{s} is anisotropic, and the parameters are assumed to be spatially dependent as a m -th order polynomial along the normal axes. To more accurately represent the spatial variation, numerical integration was used to perform the integrals in (47) using numerical quadrature. Furthermore, since the PML interfaces are assumed planar, the implementation of (47) is quite simple in the FEM routine and no special preprocessing is required. The exterior of the PML region is assumed to be a PEC wall. On this wall, a Dirichlet boundary condition is enforced.

3. Finite Element Tearing and Interconnecting Method

The Finite Element Tearing and Interconnecting Method (FETI) is a domain decomposition technique based on a hybrid variational principle. For simplicity consider a domain Ω divided into non-overlapping subdomains Ω_i . Adjacent subdomains will share common boundaries defined by Γ_{ij} . The vector electric fields and testing functions within each subdomain are

discretized separately into finite elements. Then evaluating the first variation of (47) at a stationary point yields:

$$K_i e_i = f_i \quad (48)$$

where e_i is the vector field unknowns in region Ω_i ($i = 1, 2$), K_i is the stiffness matrix, and f_i is the forcing vector in Ω_i .

The discrete fields in each subregion are constrained to enforce the continuity of the tangential electric fields across the shared boundary. Specifically, let B enforce the continuity of the discrete tangential fields across the shared boundaries $\Gamma_{i,j}$. Subsequently, using the method of Lagrange multipliers, it is desired to solve the linear system of equations

$$Ke = f \quad (49)$$

under the constraint

$$Be = 0 \quad (50)$$

where K is a block diagonal matrix defined by

$$K = \begin{bmatrix} K_1 & 0 & \cdots & 0 \\ 0 & K_2 & \cdots & 0 \\ & & \ddots & \\ 0 & \cdots & 0 & K_N \end{bmatrix}, \quad (51)$$

e and f are described as

$$e = \begin{bmatrix} e_1 \\ e_2 \\ \vdots \\ e_N \end{bmatrix}, \quad f = \begin{bmatrix} f_1 \\ f_2 \\ \vdots \\ f_N \end{bmatrix} \quad (52)$$

and B is also a block matrix representing $\hat{n} \times (\bar{e}_i - \bar{e}_j) = 0$. It is noted that B is highly sparse, and all non-zero entries are simply ± 1 . From the theory of Lagrange multipliers, the solution of this constrained linear system is equivalent to finding the stationary point of

$$f = \frac{1}{2} e^T Ke - e^T f + \lambda^T Be \quad (53)$$

where λ is the vector of Lagrange multipliers. Taking the first variation of (53) and evaluating it at the stationary point leads to the symmetric linear system of equations

$$\begin{bmatrix} K & B^T \\ B & 0 \end{bmatrix} \begin{bmatrix} e \\ \lambda \end{bmatrix} = \begin{bmatrix} f \\ 0 \end{bmatrix} \quad (54)$$

From the first row of (54), it follows that

$$e = K^{-1}(f - B^T \lambda) \quad (55)$$

combining this with the second row of (54) leads to the symmetric sparse linear system of equations

$$BK^{-1}B^T \lambda = BK^{-1}f \quad (56)$$

The parallel algorithm then proceeds as follows: *i)* K is factorized using a sparse matrix factorization method. Note that this is done completely in parallel due to the block diagonal characteristics of K defined in (51). As a result, each K_i is factorized independently and concurrently on each processor. *ii)* A complex CG algorithm is used to compute the solution for the Lagrangian vector λ from the reduced order matrix equation in (56). It is noted that the matrix vector multiplies are performed completely in parallel since the products of vectors with the matrix blocks K_i^{-1} and B_i can be performed explicitly in parallel. *iii)* Once the Lagrange multipliers are computed, the electric fields are computed in parallel from (55). It is noted that the matrix in (56) is well conditioned, and the order of the matrix is greatly reduced as compared to the order of the global matrix. As a result, the iterative scheme is expected to converge rapidly. It is also noted that if there is symmetry or repetitiveness in the geometry resulting in blocks with identical K_i , then such blocks only need to be stored and factored once on one processor. (It is noted that proper load balance should still monitored such instances).

4. Results

Initially, the effectiveness of the UPML absorbing media will be presented for the frequency-dependent analysis. Then, the efficiency of the FETI solution will be studied for FEM models with UPML. To study the effectiveness of the FETI for solving PML meshes, an air filled rectangular waveguide was initially studied. This problem was chosen since the exact solution is known. Secondly, it isolates the performance of a single wall in the discrete space. The waveguide is assumed to have a cross section of $a = 0.4$ m by $b = 0.4$ m. The TE_{01} mode is excited at one end of the waveguide, and the other end is terminated into a UPML layer. The waveguide was excited at 400 MHz which is above the TE_{01} mode cutoff frequency of 375 MHz. Initially, the waveguide length was set to 1.1 m and the depth of the PML was 0.4 m which is effectively 8 cell radii thick. First-order tetrahedral edge elements or Whitney elements were used in this study, and there was no effort to make the tetrahedral elements symmetric about any axis. We looked at the effect of varying the order of the spatial polynomial from $m = 0$ to $m = 3$. In addition κ_1 was set to 1 for the propagating mode, and effectively σ_{\max} was varied by correspondingly varying the theoretical reflection coefficient R_{th} , which is defined as [26]:

$$R_{th} = e^{-2 \frac{\sigma_{\max}}{\omega \epsilon_0} \beta_z^i d / (m+1)} \quad (57)$$

where m is the order of the spatial polynomial and d is the thickness of the PML layer in meters. Subsequently, σ_{\max} is given by:

$$\sigma_{\max} = -\omega \epsilon_0 \frac{(m+1)}{2\beta_z^i d} \ln(R_{th}) \quad (58)$$

The reflection coefficient computed numerically is illustrated in Fig. 13. Superimposed in this graph is the theoretical prediction of R_{th} . The theoretically predicted reflection coefficient is followed up to an optimal value. The case when $m = 3$ performed optimally, and provides -60 dB to -70 dB of absorption near its optimal value near $\ln(R_{th}) = -6.6$. Choosing R_{th} above this value leads to a degradation in the performance of the PML.

The parallel FETI solution method was implemented on a 32 processor Intel iPSC/860 hypercube. For scalability analysis, the physical length of the waveguide was varied from 0.8 m to 12.8 m doubling the length at each step and simultaneously doubling the number of processors. (Note that the PML depth was kept constant ($d = 0.4$ m)). At each step the number of processors used was also doubled keeping the number of elements per processor constant. This provided for a *scaled speedup* analysis. Scaled speedup provides a measure of the scalability of the algorithm by scaling the problem size with the number of processors. Scaled speedup can be determined by summing the efficiencies of each processor. This method essentially determines the amount of time it would take a single processor to solve the same problem as the multi-processor system. Finally, the order of the spatial variation was set to $m = 0$ and the conductivity was set by choosing $R_{th} = 1.367e-05$.

Table 3 summarizes the results from varying the number of processors from two to thirty-two with each processor responsible for 3072 elements. The discretization used for this problem was a simple one-way dissection. As a result, for each case there are $(P-1)$ common boundaries with 176 common edges per boundary where P is the number of processors used. The waveguide problem solution was found by solving the local problem using a direct solver while solving the global problem using an iterative solver (PCGM). The local problem could have also been found using a iterative solver but for this study a direct solver was chosen.

To compare with the FETI method, Table 4 shows the results from solving the same problem using a single node on a SGI Power Challenge using a PCG method with diagonal preconditioning. It is interesting to note that the number of iterations has dramatically increased. This is due to the fact that the FEM matrix becomes highly ill-conditioned with PML present. Interestingly, the reduced matrix resulting from the FETI solution is very well conditioned, as illustrated in Table 3.

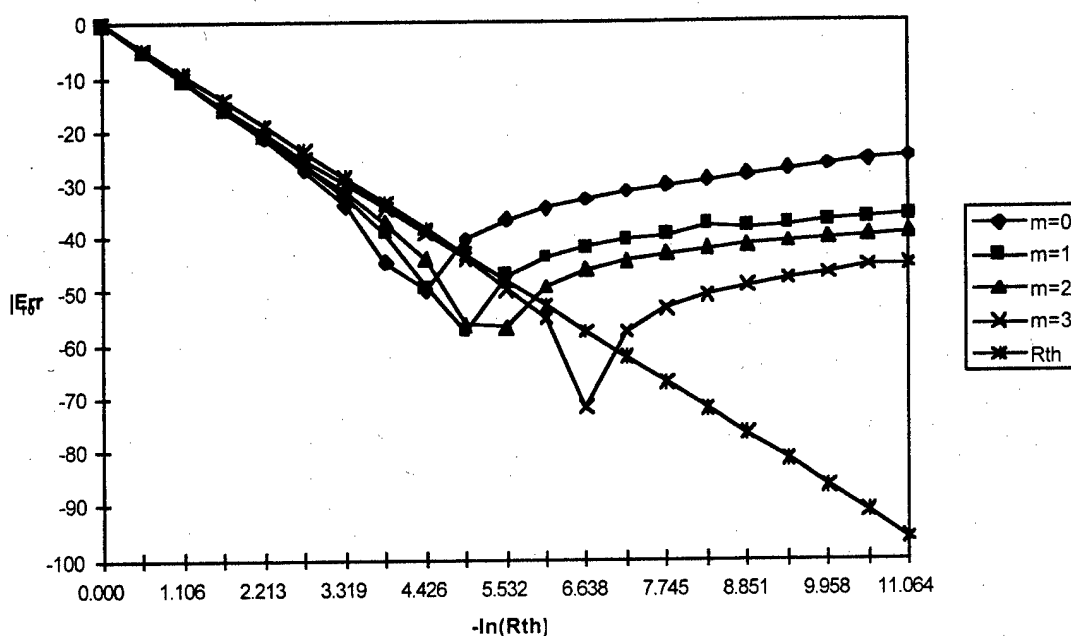


Fig. 13. Fitted reflection error for a $0.4\text{m} \times 0.4\text{m} \times 1.1\text{m}$ waveguide with a 0.4m PML for different values of the polynomial variation, m , and σ_{\max} within the PML.

Table 3. Comparison of results for the FETI algorithm with 3072 cells per Processor

Processors	2	4	8	16	32
Total number of Unknowns	6240	12656	25488	51152	102480
# of Lagrangian Multipliers	176	528	1232	2640	5456
Iterations	57	133	187	261	385
Scaled Speedup	1.27	2.21	4.99	11	24.2
Execution Time (sec)	227	378	456	567	752

Table 4. Results for waveguide problem on a Single Processor using Diagonal Preconditioning.

Total number of Unknowns	6240	12656	25488	51152	102480
Iterations	4212	6974	12028	22063	61642
Execution Time (sec)	107	394	1604	6733	45719

VI A Parallel Unconditionally Stable Finite-Element Time-Domain Algorithm

The previous section presented a parallel finite-element frequency-domain algorithm. The focus of this section is the development of a parallel finite-element time-domain algorithm. Finite element time-domain based solutions of Maxwell's equations have been developed using both implicit [46], and explicit methods [47]. For an implicit method to be competitive with an explicit method, the number of time iterations required to converge to a final solution must be significantly less, since each time iteration requires a solution of a linear system of equations. Unfortunately, the implicit finite element time-domain (FETD) methods presented in [46] are conditionally stable, and in fact, stability can lead to time steps that are *smaller* than that required by explicit FDTD methods [9]. Therefore, it becomes necessary to develop a technique that is unconditional stable. The time-dependent vector wave equation for a lossy, inhomogeneous space is written as

$$\nabla \times \frac{1}{\mu_r} \nabla \times \bar{E} + \mu_o \sigma \frac{\partial \bar{E}}{\partial t} + \frac{\epsilon_r}{c_o^2} \frac{\partial^2 \bar{E}}{\partial t^2} = -\mu_o \frac{\partial \bar{J}}{\partial t} \quad (59)$$

A variational expression is then derived from this equation. Then, expanding the field using vector finite elements leads to a linear system of equations with time dependent coefficients e

$$[T_\epsilon] \frac{1}{c_o^2} \frac{d^2 e}{dt^2} + [T_\sigma] \frac{\eta_o}{c_o} \frac{de}{dt} + [S]e = -f \quad (60)$$

A difference equation is derived using the Newmark Beta formulation, leading to the implicit formulation for the electric field

$$e^{n+1} = \left[[T_\epsilon] + \frac{1}{2} \eta_o c_o \Delta t [T_\sigma] + \beta (c_o \Delta t)^2 [S] \right]^{-1} \left\{ \left[2[T_\epsilon] - (1-2\beta)(c_o \Delta t)^2 [S] \right] e^n - \left[[T_\epsilon] - \frac{1}{2} \eta_o c_o \Delta t [T_\sigma] + \beta (c_o \Delta t)^2 [S] \right] e^{n-1} - (c_o \Delta t)^2 [\beta f^{n+1} + (1-2\beta)f^{n+1} + \beta f^{n-1}] \right\} \quad (61)$$

where β is the Newmark Beta coefficient. Performing a stability analysis, it is found that if $\beta \geq 0.25$, this implicit formulation is unconditionally stable [6]. It is further found that the optimal choice for β is 0.25, as this leads to minimal error. This is intuitive since if $\beta = 0.25$, this formulation is equivalent to that derived using a trapezoidal time-integration scheme. The principal advantage of unconditional stability is that the time step is no longer governed by the mesh quality and the resulting eigenspectrum of the linear system, but rather by the spectral content of the signal propagating through the mesh. For printed circuit applications, this has a great implication as cell sizes can easily be on the order of $0.001 \lambda_{min}$ or smaller.

A parallel algorithm was implemented to perform the implicit time-dependent solution based on the FETI algorithm described in the previous section. As expected, this has provided excellent speedups. As a demonstration of the effectiveness of the algorithm, we consider the problem of computing the resonant frequencies of a cavity loaded with a PEC wedge, as illustrated in Fig. 14. The cavity has the dimensions 1.0 m by 1.0 m by 1.5 m. The wedge has a base area of 0.2 m

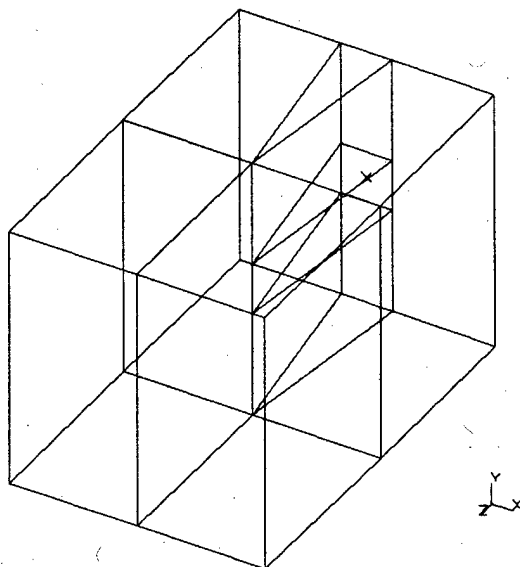


Fig. 14 A PEC Wedge in a cavity

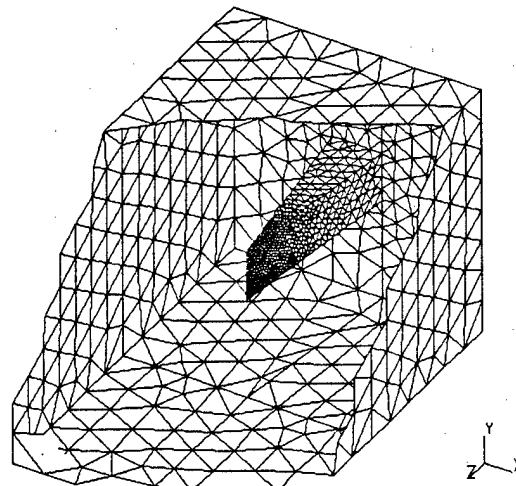
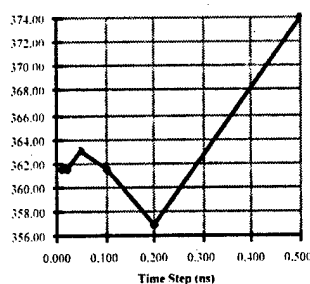
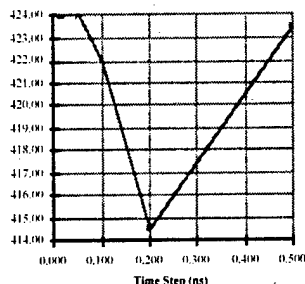


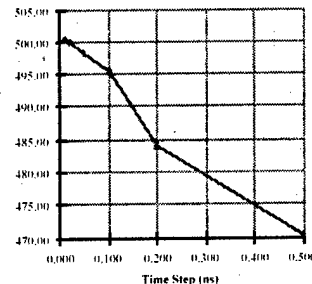
Fig. 15 Tetrahedral mesh of the surface of the wedge and cavity



(a)



(b)



(c)

Fig. 16 Variation of resonant frequency v/s the time step.

by 0.2 m and a height of 0.75 m. This problem was modeled using SDRG/I-DEAS using tetrahedral elements. The maximum element size is 0.1 m and the minimum size is 0.005 m. Near the apex of the wedge, the element sizes are very small so that the fine geometries in this region can be accurately measured. The surface mesh on part of the geometry is shown in Fig. 15.

Figures 16.(a)-(c) illustrate the variation in the resonant frequencies as the time step is increased. We notice that the error in the resonant frequency is less than 1.0 % for all values of the time step, except for the last data point. A central difference algorithm has a limit on the time step of 0.0075 ns because of stability considerations.

Figure 17 illustrates the variation of the total execution time for the time simulation as the time step is increased. It is noted that the execution time decreases as the time step is increased. This decrease in the execution time is very sharp for the smaller time steps, but as the time step is made larger, this benefit reduces. Figure 17 also illustrates the variation in the number of iterations per time step for the Conjugate Gradient algorithm versus the time step. We see that as the time step is

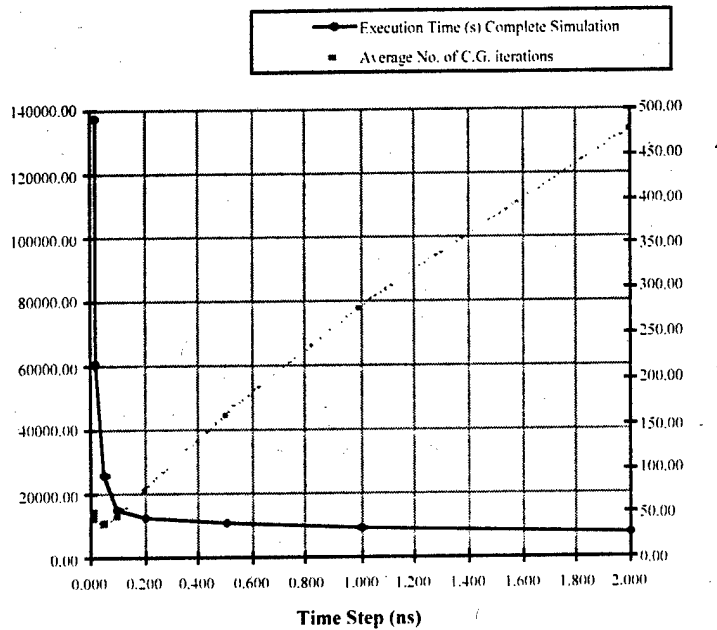


Fig. 17 Variation of Execution time and Average number of CG iterations per time step with the time step.

increased, the CG algorithm requires approximately the same number of iterations for convergence for small time steps, but this number grows almost in direct proportion to the time step. Thus, an appropriate choice for selecting the simulation time step can be made by considering both Figs. 16 and 17 to give reasonable accuracy and fast execution. For this problem, an appropriate choice for the time step would be approximately 0.1 ns. Note that this time step is more than an order of magnitude larger than the central difference algorithm stability limit and can reduce execution time for the complete simulation by that factor.

VII Orthogonal and Nonorthogonal FDTD Analysis of Periodic Structures

1. Introduction

Frequently, it is of interest to analyze the electromagnetic scattering by bodies with geometries with periodicity in one or more dimension. Some examples of applications of periodic structures are frequency selective surfaces, active grid arrays, or photonic band gap structures. Taking advantage of this periodicity can lead to greater efficiency and accuracy when solving the problem numerically.

Typically each periodic feature is referred to as a cell and the periodicity of these cells is accounted for using Floquet theory. For a normally incident plane wave, accounting for this periodicity in either an orthogonal or non-orthogonal FDTD method is quite straightforward as there is no phase shift between each periodic cell [48]. However, when a plane wave source is obliquely incident there is a cell-to-cell phase variation between corresponding points in different unit cells which causes the time-domain implementation to become more difficult.

For oblique incidence plane waves, a Floquet field mapping may be applied which results in a set of mapped fields which possess the same cell-to-cell field relations as exist for the normally incident, unmapped fields [49]. The resulting equations may add considerable complexity to the FDTD solution [50] and lead to a more stringent stability relation for higher angles of incidence. At present, the periodic methods which are available have only been applied using the orthogonal FDTD method.

In this work, the Floquet-mapped periodic FDTD equations are solved using an alternative approach referred to as the split-field update method. This technique is shown to be simple to implement and a stability analysis shows the technique to have a less strict stability criterion than previous implementations. Subsequently, the split-field update method is applied in a general curvilinear space using the non-orthogonal FDTD technique. The use of Floquet-mapped FDTD in non-orthogonal grids may lead to further computational savings due to fewer and larger cells. The split-field update technique is validated by comparison of the numerical results with measured data.

2. Formulation

The field components of a TM_z plane wave incident on a two dimensional material which is periodic in the x direction will have a phase shift of the form $e^{jk_x x}$ where $k_x = \frac{\omega \sin \theta}{v_0}$, v_0 is the speed of light in free space, and θ is the angle of propagation for the incident field. A set of auxiliary variables is introduced which implicitly accounts for this phase shift as [49]

$$P_z = \frac{E_z e^{-jk_x x}}{\eta_0}, \quad Q_x = H_x e^{-jk_x x}, \quad Q_y = H_y e^{-jk_x x}. \quad (62)$$

Substituting these expressions into Maxwell's curl equations maps the solution space such that there is no phase shift between the computed fields at like positions in each periodic cell. Now boundary conditions at the periodic boundaries consist of constraining the tangential fields on opposing boundary walls to be equivalent. The application of this mapping in orthogonal is first presented and then for non-orthogonal grids.

3. Orthogonal Grid FDTD

Substituting (62) into Maxwell's curl equations leads to:

$$j\omega \frac{\epsilon_r P_z}{v_o} = \frac{\partial Q_y}{\partial x} - \frac{\partial Q_x}{\partial y} + j\omega \frac{\sin \theta}{v_o} Q_y, \quad (63)$$

$$j\omega \frac{\mu_r Q_x}{v_o} = -\frac{\partial P_z}{\partial y}, \quad (64)$$

$$j\omega \frac{\mu_r Q_y}{v_o} = \frac{\partial P_z}{\partial x} + j\omega \frac{\sin \theta}{v_o} P_z \quad (65)$$

Notice that the substitution of (62) has produced extra terms (denoted by brackets) on the right hand side of (63) and (65). When (63) and (65) are discretized, the presence of these extra terms leads to difficulty. One difficulty arises due to the appearance of the time derivative ($j\omega \Rightarrow \frac{\partial}{\partial t}$) on both sides of these equations. Another difficulty arises because the right hand sides are no longer spatially aligned. These difficulties may be overcome by introducing dual grids in time and multiple grids in space [50].

In this work an alternate approach is taken which is numerically stable, efficient, and applicable in either orthogonal or non-orthogonal grids. The technique used here will be referred to as the split-field update method. Equation (63) is now 'split' into two parts by defining $P_z = P_z^a + P_z^b$ where

$$j\omega \frac{\epsilon_r P_z^a}{v_o} = \frac{\partial Q_y}{\partial x} - \frac{\partial Q_x}{\partial y}, \quad (66)$$

$$P_z^b = \frac{\sin \theta}{\epsilon_r} Q_y. \quad (67)$$

Equation (65) is split similarly by defining $Q_y = Q_y^a + Q_y^b$ where

$$j\omega \frac{\mu_r Q_y^a}{v_o} = \frac{\partial P_z}{\partial x} \quad (68)$$

$$Q_y^b = \frac{\sin \theta}{\mu_r} P_z. \quad (69)$$

Substituting the split forms of P_z and Q_y along with (69) into (67) and solving for P_z then gives

$$P_z = \frac{P_z^a}{1 - \frac{\sin^2 \theta}{\epsilon_r \mu_r}} + \frac{\sin \theta}{\epsilon_r - \frac{\sin^2 \theta}{\mu_r}} Q_y^a \quad (70)$$

Equations (64), (66), and (68) and (70) are discretized using a spatially interleaved Yee lattice. Furthermore, a dual time grid is introduced such that each field component of both P and Q is computed at each half time step. Note that the time derivatives are applied using central differencing in time as usual, but now these updates are computed at each half time step. Spatial alignment required in (70) is accomplished by field averaging which provides second order accurate results without resorting to multiple spatial grids. The resultant update equations are

$$P_{z,i,j}^{a^n} = P_{z,i,j}^{a^{n-1}} + d_{i,j}^x \left(Q_{y,i,j}^{n-\frac{1}{2}} - Q_{y,i-1,j}^{n-\frac{1}{2}} \right) - d_{i,j}^y \left(Q_{x,i,j}^{n-\frac{1}{2}} - Q_{x,i,j-1}^{n-\frac{1}{2}} \right) \quad (71)$$

$$Q_{x,i,j}^n = Q_{x,i,j}^{n-1} + b_{i,j}^y \left(P_{z,i,j+1}^{n-\frac{1}{2}} - P_{z,i,j}^{n-\frac{1}{2}} \right) \quad (72)$$

$$Q_{y,i,j}^n = Q_{y,i,j}^{n-1} + b_{i,j}^x \left(P_{z,i+1,j}^{n-\frac{1}{2}} - P_{z,i,j}^{n-\frac{1}{2}} \right) \quad (73)$$

$$P_{z,i,j}^n = \frac{P_{z,i,j}^{a^n} + \frac{\sin \theta}{2\epsilon_r} (Q_{y,i,j}^{a^n} + Q_{y,i-1,j}^{a^n})}{1 - \frac{\sin^2 \theta}{\epsilon_r \mu_r}} \quad (74)$$

$$Q_y^b = \frac{\sin \theta}{\mu_r} (P_{z,i+1,j}^n + P_{z,i,j}^n) \quad (75)$$

where

$$d_{i,j}^x = \frac{\Delta t}{\epsilon_r \Delta x}, \quad d_{i,j}^y = \frac{\Delta t}{\epsilon_r \Delta y}, \quad b_{i,j}^x = \frac{\Delta t}{\mu_r \Delta x}, \quad b_{i,j}^y = \frac{\Delta t}{\mu_r \Delta y}$$

Implementation of (71) through (75) has proven that this technique is stable for all angles under 90 degrees.

An exact stability relationship was derived for these update equations [51]:

$$\Delta t < \frac{1}{v_o} \frac{\Delta x \cos^2 \theta}{|\sin \theta| \sin \xi \cos \xi + \sqrt{\sin^2 \theta \sin^2 \xi \cos^2 \xi + (\sin^2 \xi + a) \cos^2 \theta}} \quad (76)$$

where

$$\xi = \cos^{-1} \left(\frac{1}{2} \sqrt{\frac{1 + \sin^2 \theta (4a + 2) - \sqrt{\sin^2 \theta (a - \sin^2 \theta) + 1}}{\sin^2 \theta (2 + 3a) + a}} \right) \quad (77)$$

and $a = (\Delta x / \Delta y)^2$. It is noted that this stability criterion is must less stringent than that of the algorithm in [49] at higher angles of incidence. In fact, near grazing the time step can be increased by as much as a factor of 3.

4. Non-Orthogonal Grid FDTD

Next, the split-field update method is applied to a two-dimensional non-orthogonal grid. To this end, it is assumed that the grid is structured, but irregular and non-orthogonal. Each cell is locally defined by a curvilinear coordinate axis, defined as (u_1, u_2, u_3) . The axis is defined on a local basis by the unitary vectors $\hat{a}_1, \hat{a}_2, \hat{a}_3$, where \hat{a}_3 is orthogonal to the u_1, u_2 plane. In the general curvilinear space, the covariant field values are tangential to the unitary vectors and are designated by subscripts. The contravariant field vectors are normal to the cell faces whose edges are defined by the unitary vectors and are designated by superscripts. In the orthogonal space, a mapping of the form in (40) was assumed. This mapping is projected into the general curvilinear space as:

$$\begin{aligned} P_3 &= \frac{E_3 e^{-j(\beta_1 u_1 + \beta_2 u_2)}}{\eta_o}, \\ Q_1 &= H_1 e^{-j(\beta_1 u_1 + \beta_2 u_2)}, \\ Q_2 &= H_2 e^{-j(\beta_1 u_1 + \beta_2 u_2)}, \end{aligned} \quad (78)$$

where, $\beta_1 = k_x \cdot a_{1x}$, $\beta_2 = k_x \cdot a_{2x}$, and a_{1x} and a_{2x} represent the x -directed component of the normalized unitary vectors \hat{a}_1 and \hat{a}_2 , respectively. An equivalent expression to (78) is also used for the contravariant field components.

The mapped fields in (78) are then inserted into the differential form of Maxwell's equations in general curvilinear coordinates [52]. For the TM_z case, this leads to:

$$j\omega \frac{\epsilon_r P^3}{v_o} = \frac{1}{\sqrt{g}} \left(\frac{\partial Q_2}{\partial u_1} - \frac{\partial Q_1}{\partial u_2} \right) + j\omega \frac{\sin \theta}{v_o \sqrt{g}} a_{1x} Q_2 - j\omega \frac{\sin \theta}{v_o \sqrt{g}} a_{2x} Q_1, \quad (79)$$

$$j\omega \frac{\mu_r Q^1}{v_o} = -\frac{1}{\sqrt{g}} \frac{\partial P_3}{\partial u_2} - j\omega \frac{\sin \theta}{v_o \sqrt{g}} a_{2x} P_3, \quad (80)$$

$$j\omega \frac{\mu_r Q^2}{v_o} = \frac{1}{\sqrt{g}} \frac{\partial P_3}{\partial u_1} + j\omega \frac{\sin \theta}{v_o \sqrt{g}} a_{1x} P_3. \quad (81)$$

Note that the substitution of (78) has resulted in extra terms (denoted by brackets) on the right-hand-side of (79)-(81). Once again, these terms are handled efficiently via a field splitting. Specifically, let $P^3 = P^{3a} + P^{3b}$, $Q^1 = Q^{1a} + Q^{1b}$, and $Q^2 = Q^{2a} + Q^{2b}$, where

$$j\omega \frac{\epsilon_r P^{3a}}{v_o} = \frac{1}{\sqrt{g}} \left(\frac{\partial Q_2}{\partial u_1} - \frac{\partial Q_1}{\partial u_2} \right), \quad P^{3b} = \frac{\sin \theta}{\epsilon_r \sqrt{g}} a_{1x} Q_2 - \frac{\sin \theta}{\epsilon_r \sqrt{g}} a_{2x} Q_1, \quad (82)$$

$$j\omega \frac{\mu_r Q^{1a}}{v_o} = -\frac{1}{\sqrt{g}} \frac{\partial P_3}{\partial u_2}, \quad Q^{1b} = -\frac{\sin \theta}{\mu_r \sqrt{g}} a_{2x} P_3, \quad (83)$$

$$j\omega \frac{\mu_r Q^{2a}}{v_o} = \frac{1}{\sqrt{g}} \frac{\partial P_3}{\partial u_1}, \quad Q^{2b} = \frac{\sin \theta}{\mu_r \sqrt{g}} a_{1x} P_3. \quad (84)$$

Finally, each covariant component is projected from the contravariant field components through the mapping

$$F_i = \sum_{j=1}^2 g_{ij} F^j \quad (85)$$

where $g_{ij} = \hat{a}_i \cdot \hat{a}_j$ and $\sqrt{g} = \hat{a}_3 \cdot (\hat{a}_1 \times \hat{a}_2)$.

To solve the split field equations in (82) and (83), through the manipulation of terms, it can be shown that

$$P^3 = \frac{P^{3a} + \frac{\sin \theta}{\epsilon_r \sqrt{g}} a_{1x} Q_{2a} - \frac{\sin \theta}{\epsilon_r \sqrt{g}} a_{2x} Q_{1a}}{1 - \sin \theta \left(\frac{a_{2x}}{\sqrt{g}} M_1 - \frac{a_{1x}}{\sqrt{g}} M_2 \right)} \quad (86)$$

where

$$M_1 = \frac{a_{2x} g_{11} \sin \theta}{\epsilon_r \mu_r \sqrt{g}} - \frac{a_{1x} g_{21} \sin \theta}{\epsilon_r \mu_r \sqrt{g}}, \quad M_2 = \frac{a_{2x} g_{12} \sin \theta}{\epsilon_r \mu_r \sqrt{g}} - \frac{a_{1x} g_{22} \sin \theta}{\epsilon_r \mu_r \sqrt{g}}. \quad (87)$$

and hence eliminating P^{3b} , Q^{1b} , and Q^{2b} .

Finally, (82) through (87) can be implemented in a discrete space in a similar manner as that presented for the orthogonal grid algorithm. Specifically, both P and Q are updated at every half time step. Then, P^{3a} , Q^{1a} , and Q^{2a} are updated using (82) - (87). It is noted that $P_3 = P^3$ due to the assumption of a two-dimensional geometry.

5. UPML Boundary Condition

In both the orthogonal and the non-orthogonal grid codes, the uniaxial PML method was successfully employed to terminate the non-periodic boundaries. This was based on a simple extension of the work in [14, 51].

6. Validation

To validate both the non-orthogonal and orthogonal formulations, the algorithms were applied to the analysis of a photonic bandgap (PBG) structure. The results were then compared to measured results provided by Georgia Tech Research Institute, in Atlanta, GA. The geometry under study is illustrated in Figure 18. Each unit cell consists of four infinitely long dielectric rods with a radius of $a = 2$ mm and a dielectric constant of $\epsilon_r = 4.2$. The rods are arranged in a square lattice such that the center-to-center separation distance is equal to the unit cell width where $b = 9.0$ mm. Simulations were run at angles of incidence of 0 to 50 degrees where experimental data (transmission coefficient) was provided.

This structure was analyzed using both the orthogonal and non-orthogonal implementations formulated in this work. The orthogonal FDTD code is based on (49) through (53) with each

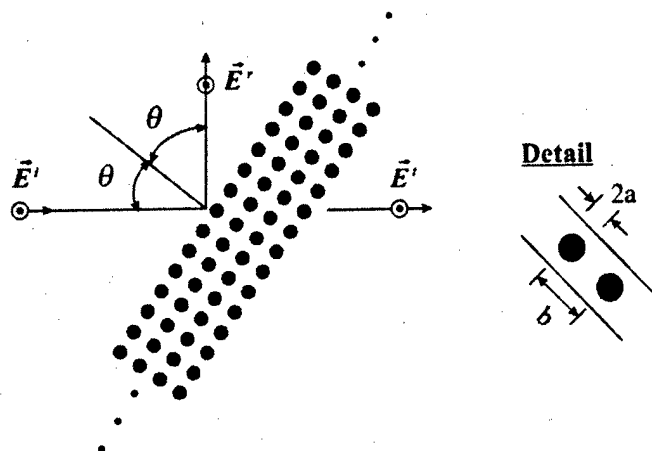


Fig. 18 Cross-section of a slab of two-dimensional photonic band-gap material.

dielectric rod discretized at 16 cells ($\Delta x = \Delta y = 0.25$ mm) across the diameter of rod. The grid dimensions were 39×229 including a 10 cell PML region at the two y -directed walls. Test were run which showed that the numerical solution had converged at this discretization. In the non-orthogonal FDTD based on (60) through (65) only six cells across the diameter of the dielectric rods were used and the grid dimensions in were 19×105 cells including a 10 cell PML region. For each case, the PML parameters were optimally chosen based on [14, 51].

Figures 19 illustrate the level of agreement between the two numerical methods as well as with the measured data for a TM_z incident plane wave incident at 20° off normal. The level of agreement is quite good and a clear bandgap of at least 10 dB is indicated. The error is very small for either case and probably within the margin of measurable accuracy. The orthogonal implementation of this method was stable for all angles of incidence less than 90° . The non-orthogonal method was stable for angles of incidence less than 60° . For angles greater than 60° the method did go unstable in the very late time.

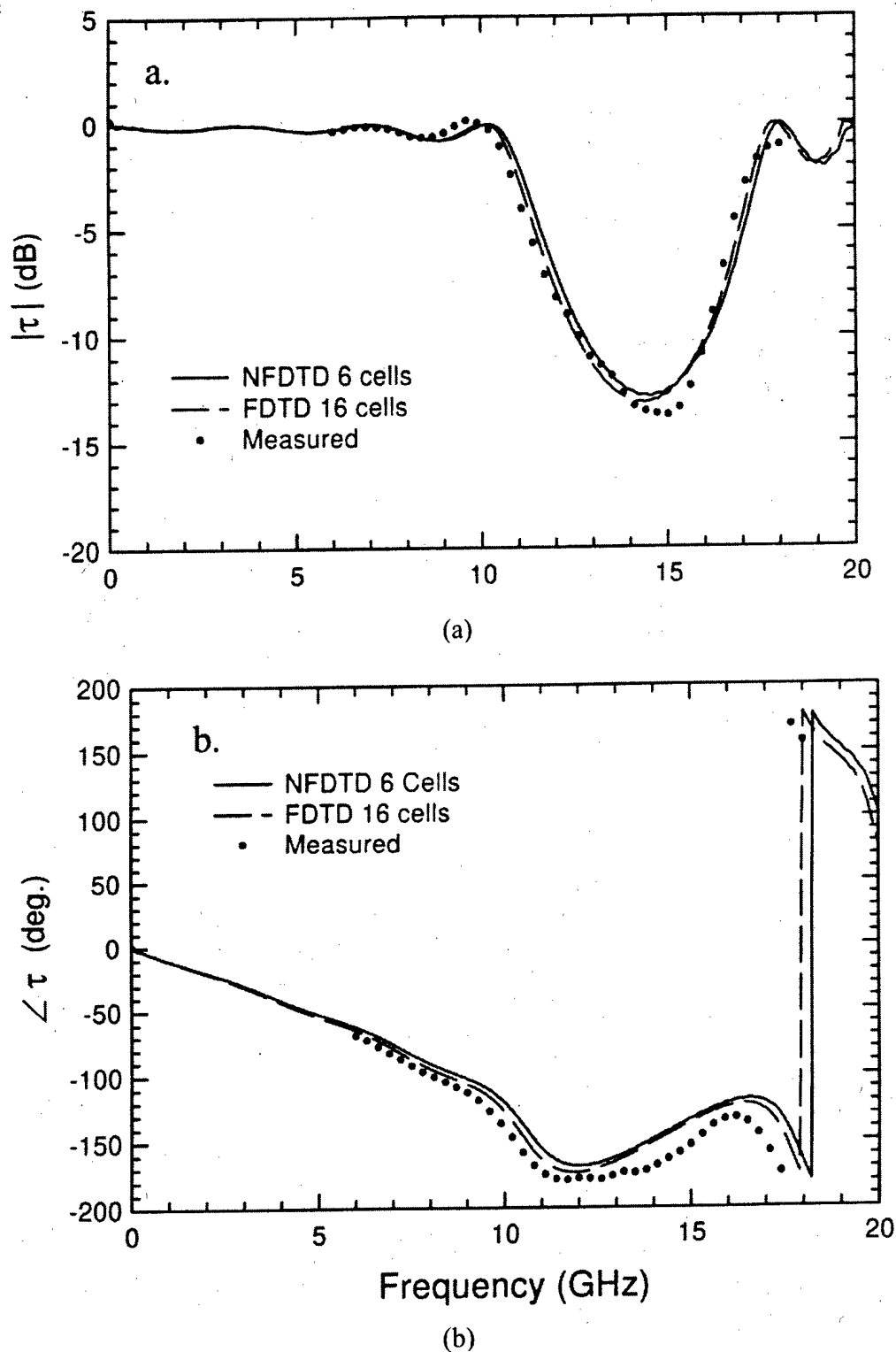


Fig. 19 Transmission coefficient of four rod deep photonic bandgap structure for a TM_z plane wave incident at 20 degrees. (a) magnitude, (b) phase. Periodic cell is 9mm wide and rod diameter is 4 mm, and $\epsilon_r = 4.2$.

VIII Incorporating the State Variable Technique into the FDTD and PGY Methods for Modeling Linear and Nonlinear Devices

1. Introduction

The formulations for modeling lumped elements using the FDTD method have been developed for several years [53], [54] and the numerical results computed by the FDTD method are in excellent agreement with those computed by other CAD tools such as SPICE. Research for connecting the SPICE with the FDTD analysis has also been conducted [55]. To further extend the applications of the FDTD method, the state-variable technique has recently been incorporated into the FDTD algorithm in analyzing the small signal equivalent circuits for microwave active devices [56, 57] and the nonlinear large signal model for GaAs MESFET amplifiers [58]. There are two basic techniques for modeling microwave active devices. The first technique is to replace the active regions of the devices by equivalent current sources with parallel FDTD cell capacitance's. The second technique is to replace the active regions of the devices by equivalent voltage sources with series FDTD cell inductance's. These two techniques are referred as the current-source approach [56] and the voltage source approach [57], respectively. It is important to realize that the current-source and the voltage-source approaches are dual. The former is based on Ampere's law and the latter is based on Faraday's law. The current-source (CS) approach has an advantage over the voltage-source (VS) approach in the sense that the CS approach provides more physical insight to the problem. For instance, when modeling the active regions, such as the gate port and the drain port, of a microwave active device, those regions are usually divided into several FDTD cells. Then the net current sources and the net capacitances at those regions are just the sums of the individual current source and capacitance for each cell respectively (since the sources and capacitances are in parallel). The VS approach does not yield similar physical insight [57]. On the other hand, the VS approach can sometimes simplify the state-variable model for the equivalent circuit of a microwave active device by reducing the number of the state variables that are to be solved [58]. This is the main advantage for using the VS approach. Due to the straightforward implementation and physical understanding of the CS approach, this paper will follow the formulation presented in [56]. The CS approach will be briefly reviewed in Section 2.

There is no doubt that the major task for modeling a nonlinear device is to solve for a set of nonlinear equations that describe the characteristics of the device. One of the most popular algorithms is the Newton-Raphson algorithm. It is obvious that a set of nonlinear differential equations needs to be used to describe the nonlinear state-variable model for the device. This set of differential equations can be transformed into a set of nonlinear algebraic equations by using the predictor-corrector algorithm [59]. The Newton-Raphson algorithm is then applied to solve for this set of nonlinear algebraic equations. In order to assure that the solutions for the nonlinear equations always converge to correct values, a globally convergent method based on the Newton's

method [60] is employed in this paper. Some of the basic concepts for this convergent method will be discussed in Section III. To consolidate the validity for the use of state-variable technique along with the FDTD algorithm in performing full-wave analyses on microwave circuits, several numerical examples will be presented in Section IV. Finally, the conclusion is drawn in Section V.

2. The Current-Source Approach

For the sake of discussion and simplicity, it is assumed that the lumped elements are z-directed. The integral form for Ampere's law is

$$\oint_C \vec{H} \cdot d\vec{\ell} = \frac{d}{dt} \iint_S \epsilon \vec{E} \cdot d\vec{s} + \iint_S \vec{J}(\vec{E}) \cdot d\vec{s} \quad (88)$$

Assume a lumped device is placed on an edge of the primary grid. Then (88) is applied to the secondary grid face through which the edge passes. To represent this more conveniently, (88) is rewritten as

$$I_{tot} = C_F \frac{dV}{dt} + I_{dev}(V) \quad (89)$$

where I_{tot} is the total current given by the line integral in (89) and is performed about secondary grid face, $C_F = \epsilon A / \Delta z$, where A is the cross area of the face and Δz is the length of the device loaded edge, and $I_{dev}(V)$ is the current flowing through the device. The equivalent circuit representing (89) is illustrated in Fig. 20. Thus, given I_{tot} , a state variable approach will be used to solve (89) for the voltage V . Subsequently, V will be used to calculate the electric field on the edge.

3. State-Variable Solution

A state variable method will be used to solve for the device current and the port voltage as illustrated in Fig. 20. The means by which the solution is derived will differ for linear and nonlinear devices. Initially, assume that the edge is loaded with a linear device, such as a lumped passive circuit. In such a case, the state equation can be generically stated as:

$$\dot{x} = Ax(t) + bu(t) \quad (90)$$

where x is the state-variable vector, A is a square matrix, b is a vector associated with the excitation $u(t)$. There exist well-known analytical solutions to (5) for canonical problems [59]. However, (5) is solved numerically for sake of generality. Using the second-order finite-difference scheme, (5) is written as

$$\left(I - \frac{\Delta t}{2} A \right) x^{n+1} = \left(I + \frac{\Delta t}{2} A \right) x^n + \frac{\Delta t}{2} b(u^{n+1} + u^n) \quad (91)$$

where I is an identity matrix and the superscript indicates the time step. Equation (91) is an implicit scheme. Although, the order of A is assumed to be small can be solved using LU factorization. It should be noted that if there is more than one source then b will become a matrix.

It can be shown that in some instances, directly incorporating (91) into the FDTD algorithm can lead to instability. For example, terminating a microstrip line by a linear inductive load with a very small inductance can lead to instability. To guarantee a stable solution for all linear networks, the first-order backward scheme (Euler's algorithm) can be used. This leads to

$$(I - \Delta t A)x^{n+1} = x^n + \Delta t b u^{n+1}. \quad (92)$$

For the nonlinear case, the state equation is written in the form of [59]

$$\dot{x} = f(x, u). \quad (93)$$

To solve the nonlinear state equation, the predictor-corrector algorithm coupled with the Newton-Raphson algorithm is used. In particular, the first-order Adams-Bashforth predictor and the first-order Adams-Moulton corrector [59] are used:

predictor:

$$x^{n+1,(0)} = x^n + \Delta t f(x^n, u^n) \quad (94.a)$$

corrector:

$$x^{n+1,(j)} = x^n + \Delta t f(x^{n+1,(j-1)}, u^{n+1}) \quad (94.b)$$

where the superscript in the parenthesis designates the j^{th} iteration at the $n+1$ time step. Notice that (94.a) is an explicit algorithm while (94.b) is an implicit one. Note also that the set of differential equations (93) has been transformed into a set of algebraic equations in (94.a) and (94.b). Other higher order predictor-corrector algorithms could also be used. However, the absolute stability regions for those higher-order algorithms are very restrictive [59]. It is found that the use of the second-order Adams-Bashforth predictor and the use of the second-order Adams-Moulton corrector will lead to late time instability when they are applied to solve the nonlinear state equations for the large signal model of a GaAs MESFET amplifier. It is important to realize that the predictor-corrector algorithm itself can be used to solve for a set of nonlinear differential equations without the aide of the Newton-Raphson algorithm. However, a systematic strategy should be used to assure the convergence of the solutions to the nonlinear differential equations. A globally convergent method was proposed in [60] and is used in this paper.

The state equation (93) can be written as

$$\dot{x} - f(x, u) = 0. \quad (95)$$

Applying the first-order Adams-Moulton algorithm (94.a) to (95) leads to

$$F(x^{n+1}, u^{n+1}) = x^{n+1} - x^n - \Delta t f(x^{n+1}, u^{n+1}) = 0. \quad (96)$$

Expanding (96) into a Taylor's series yields solutions for the state variables at the $n+1$ time step [61], namely

$$J\delta x = -F(x^{n+1}, u^{n+1}) \quad (97.a)$$

$$x_{\text{new}}^{n+1} = x_{\text{old}}^{n+1} + \delta x. \quad (97.b)$$

where J is the Jacobian matrix. Note that the predictor (94.a) can be used as an initial guess for x_{old} in the Newton-Raphson algorithm.

The problem of solving the set of nonlinear equations (96) is the same as that for solving an unconstrained minimization problem of the form

$$g = \frac{1}{2} F \cdot F. \quad (98)$$

From a geometrical standpoint, it is obvious that the step δx should lead the function g to its descent direction at each iteration. Due to the quadratic convergence of the Newton method, it is always a good idea to try the full Newton step first. If the solution is not close enough to the minimum of g , the full Newton step may not necessarily decrease the function [60, 61]. However, since the Newton step is a descent direction for g , it is guaranteed that an acceptable step can be found for reducing the function by backtracking along the Newton direction. The backtracking algorithm is based on line searches. The solution (97.b) is then rewritten as

$$x_{new}^{n+1} = x_{old}^{n+1} + \lambda p, \quad 0 < \lambda \leq 1 \quad (99)$$

where $p = \delta x$. It is not sufficient to require merely that $g(x_{new}^{n+1}) < g(x_{old}^{n+1})$ since this criterion can fail to converge to a minimum of g [61]. A better strategy is to require the average rate of decrease of g be some fraction a of the initial rate of decrease $\nabla g \cdot p$. Mathematically, this is written as [60, 61]

$$g(x_{new}^{n+1}) \leq g(x_{old}^{n+1}) + a \nabla g \cdot (x_{new}^{n+1} - x_{old}^{n+1}), \quad 0 < a < 1. \quad (100)$$

Typically a good choice for a is 10^{-4} [61].

Next, the backtracking algorithm must be developed. The strategy for a useful and practical backtracking routine is to define the function [60, 61]

$$u(\lambda) = g(x_{old}^{n+1} + \lambda p) \quad (101)$$

so that

$$u'(\lambda) = \nabla g \cdot p. \quad (102)$$

The function $u(\lambda)$ is modeled with the most current information if a backtrack is needed and λ is chosen to minimize the model [61]. As mentioned earlier, the first step is always the full Newton step $\lambda = 1$. If this step does not meet the criterion in (100), a quadratic model is used to compute the appropriate value for λ . That is [60]:

$$u(\lambda) \approx [u(1) - u(0) - u'(0)]\lambda^2 + u'(0)\lambda + u(0). \quad (103)$$

Notice that $u(0)$ and $u'(0)$ are known and $u(1)$ has just been computed. Taking the derivative of (103) and setting the derivative to zero yields the minimum point for (103) [60]

$$\lambda = -\frac{u'(0)}{2[u(1) - u(0) - u'(0)]}. \quad (104)$$

If (104) still does not satisfy (100), subsequent backtracks will be needed. For the subsequent backtracks, $u(\lambda)$ is modeled as a cubic function [60]

$$u_{\text{cubic}}(\lambda) = a\lambda^3 + b\lambda^2 + u'(0)\lambda + u(0). \quad (105)$$

where

$$\begin{bmatrix} a \\ b \end{bmatrix} = \frac{1}{\lambda_1 - \lambda_2} \begin{bmatrix} 1/\lambda_1^2 & -1/\lambda_2^2 \\ -\lambda_2/\lambda_1^2 & \lambda_1/\lambda_2^2 \end{bmatrix} \begin{bmatrix} u(\lambda_1) - u'(0)\lambda_1 - u(0) \\ u(\lambda_2) - u'(0)\lambda_2 - u(0) \end{bmatrix}. \quad (106)$$

λ_1 and λ_2 are the most recent previous two values for λ . The minimum point for the cubic model in (105) is [60]

$$\lambda = \frac{-b + \sqrt{b^2 - 3au'(0)}}{3a}. \quad (107)$$

To avoid extremely small steps, a lower bound of 0.1 and an upper bound of 0.5 should be set for λ [60].

4. Linear Loads

The state variable equations can be easily derived for linear loads. For example, consider single lumped element terminations such as a resistor R , a capacitor C , or inductor L . The state variable equations would hence be:

Linear Resistor:

$$\dot{v}_{C_F} = -\frac{1}{RC_F}v_{C_F} + \frac{1}{C_F}I_{\text{tot}} \quad (108.a)$$

Linear Inductor:

$$\begin{bmatrix} \dot{v}_{C_F} \\ \dot{i}_L \end{bmatrix} = \begin{bmatrix} 0 & -\frac{1}{C_F} \\ \frac{1}{L} & 0 \end{bmatrix} \begin{bmatrix} v_{C_F} \\ i_L \end{bmatrix} + \begin{bmatrix} \frac{1}{C_F} \\ 0 \end{bmatrix} I_{\text{tot}} \quad (108.b)$$

Linear Capacitor:

$$\dot{v}_{C_F} = \frac{1}{C + C_F}I_{\text{tot}}. \quad (108.c)$$

It is noted that for a network of linear lumped elements, state variable equations could be similarly derived.

A Linear Amplifier

A more interesting example of a linear load would be a linear amplifier. Specifically, consider the small signal analysis of a GaAs MESFET amplifier. The equivalent circuit for this device is illustrated in Fig. 21. The state equation in (90) was used, with the exception that b is now a matrix B . To this end, from the circuit in Figs. 20 and 21 it can be shown that:

$$x = \begin{bmatrix} v_{C_F} & v_{C_{gs}} & v_{C_{gd}} & v_{C_{ds}} & v_{C_{DF}} & i_{L_g} & i_{L_s} \end{bmatrix}^T, \quad (109.a)$$

$$A = \begin{bmatrix} 0 & 0 & 0 & 0 & 0 & -1/C_{GF} & 0 \\ 0 & -1/R_i C_{gs} & 1/R_i C_{gs} & 1/R_i C_{gs} & 0 & 0 & 0 \\ 0 & 1/R_i C_{gd} & -1/R_i C_{gd} & -1/R_i C_{gd} & 0 & 1/C_{gd} & 0 \\ 0 & (1-g_m R_i)/R_i C_{ds} & -1/R_i C_{ds} & -1/R_{ids} C_{ds} & 0 & 1/C_{ds} & -1/C_{ds} \\ 0 & 0 & 0 & 0 & 0 & 0 & 1/C_{DF} \\ L_{ds}/L_T & 0 & -L_{ds}/L_T & -L_d/L_T & -L_s/L_T & -L_{1g}/L_T & L_{2g}/L_T \\ L_s/L_T & 0 & -L_s/L_T & L_g/L_T & -L_{gs}/L_T & L_{1d}/L_T & -L_{2d}/L_T \end{bmatrix}, \quad (109.b)$$

$$B = \begin{bmatrix} 1/C_{GF} & 0 \\ 0 & 0 \\ 0 & 0 \\ 0 & 0 \\ 0 & 1/C_{DF} \\ 0 & 0 \\ 0 & 0 \end{bmatrix}, \quad u(t) = \begin{bmatrix} I_{Gate}(t) \\ I_{Drain}(t) \end{bmatrix}. \quad (109.c)$$

C_{GF} and C_{DF} are the net cell capacitances at the gate port and the drain port, respectively. Specifically, assuming that the drain and gate ports are distributed over a number of cells, these represent the total networked cell capacitance, with each computed as in (89). The quantities in the excitation vector I_{Gate} and I_{Drain} are the net equivalent current sources computed by the line integrations of the magnetic fields about the gate port and the drain port, respectively. Some of the other elements in A are defined as:

$$\begin{aligned} L_{ds} &= L_d + L_s, & L_{gs} &= L_g + L_s, & R_{ids} &= R_i R_{ds} / (R_i + R_{ds}), \\ L_{1g} &= R_g L_d + R_g L_s + R_s L_d, & L_{2g} &= R_s L_d - R_d L_s, \\ L_{1d} &= R_s L_g - R_g L_s, & L_{2d} &= R_d L_g + R_d L_s + R_s L_g, \\ L_T &= L_g L_d + L_g L_s + L_d L_s. \end{aligned} \quad (110)$$

As an example, a GaAs MESFET was simulated using the FDTD algorithm. The geometry of the device is illustrated in Fig. 22. The amplifier was matched at 6 GHz. For this example, the circuit parameters were chosen yielding S-parameters at 6 GHz:

$$S_{11} = 0.636 \angle -171.3^\circ, \quad S_{12} = 0.069 \angle 16.3^\circ, \quad S_{21} = 2.061 \angle 28.63^\circ, \quad S_{22} = 0.524 \angle -95.73^\circ$$

For these S-parameters, the transistor is unconditionally stable and a simultaneous conjugate match is possible. Balanced shunt stubs and series lines are used to design the input and output matching networks. The maximum transducer gain for the amplifier is 11.137 dB. The layout is illustrated in Fig. 22. The gate and drain ports of the transistor are replaced by equivalent current sources, as illustrated in Fig. 20. These circuits are loaded with the small signal equivalent model in Fig. 21. The ports actually span the entire width of the strip. Thus, I_{Gate} and I_{Drain} represent the total current entering the gate and drain ports. This can be done by adding the currents flowing

along each edge of the port, as calculated by the line integrals of the magnetic field, or by calculating the line integral about the entire port. Similarly, the gate and drain capacitance are calculated as the total parallel capacitance across the port width. The source pads are terminated to ground by a via.

Equation (91) was used to solve for the state model of the small signal circuit. The device was excited by a broad band source and the S-parameters were then extracted over a broad frequency range. These results are illustrated in Fig. 23. The results are also overlaid with the computation done using an empirical based analysis using HP-EESOF™, which modeled both the linear MESFET amplifier with the same circuit parameters and the microstrip circuit. The results compare amazingly well.

5. Nonlinear Loads

To demonstrate the nonlinear solution of the state-variable equations, two examples will be illustrated. A nonlinear diode and a nonlinear MESFET amplifier. The equivalent circuit used for the nonlinear diode is illustrated in Fig. 24 [59]. The governing equations for this model are:

$$I_d = I_o \left(e^{\frac{qv_{c_{dp}}}{Mk_p T}} - 1 \right), \quad C_{dp} = \frac{D}{(v_z - v_{C_{dp}})^p}, \quad C_{df} = \frac{q}{2\pi Mk_b TF} I_o e^{\frac{qv_{c_{dp}}}{Mk_p T}}. \quad (111)$$

This is described in detail in [59]. The state variables for this model are $v_{C_{dp}}$, v_{C_F} , and i_L . The state equation derived from the circuit in Fig. 24 is then:

$$\dot{v}_{C_F} = -\frac{1}{C_F + C_{pack}} i_L + \frac{1}{C_F + C_{pack}} I_{tot}. \quad (112.a)$$

$$\dot{v}_{C_{dp}} = \frac{-2\pi Mk_b TF (v_z - v_{C_{dp}})^p I_o (e^{\frac{qv_{c_{dp}}}{Mk_b T}} - 1) + 2\pi Mk_b TF (v_z - v_{C_{dp}})^p i_L}{(v_z - v_{C_{dp}})^p q I_o (e^{\frac{qv_{c_{dp}}}{Mk_b T}} - 1) + D 2\pi Mk_b TF}. \quad (112.b)$$

$$i_L = \frac{1}{L_{pack}} v_{C_F} - \frac{1}{L_{pack}} v_{C_{dp}} - \frac{R_B}{L_{pack}} i_L. \quad (112.c)$$

This set of nonlinear differential equations is solved using the algorithm described in Section 3.

As a simple example, a 50 Ω microstrip line was terminated by a nonlinear diode. The dimensions of the uniform microstrip line are identical to that feeding the MESFET amplifier example. The nonlinear model illustrated in Fig. 24 was used with $tol = 10^{-4}$, $D = 10^{-12}$, $I_o = 1$ pA, $v_z = 0.7$ V, $T = 298$ K, $p = 0.5$, $M = 1.179$, $F = 1$ GHz, $C_F = 5.9976 \times 10^{-15}$ F, $L_{pack} = 10$ pH, $C_{pack} = 0.1$ pF, and $R_B = 0.1$ Ω . The results of the FDTD simulation are illustrated in Fig. 25. A 2 V sinusoidal voltage pulse with a frequency of 10 GHz is used to excite

the microstrip line. The amplitude of the pulse is ramped up using a half-Gaussian pulse to avoid high-frequency transients. It is observed from Fig. 25 that the voltage across the diode is clamped at about 0.7 V.

The final example is that of a nonlinear MESFET amplifier. The geometry of the amplifier is that of the linear amplifier presented in Fig. 22. The equivalent circuit used is also that of Fig. 21. However, the voltage-controlled current source I_{ds} and the gate to source capacitor C_{gs} are now treated as nonlinear terms. Specifically, [58]

$$I_{ds}(v_{C_{gs}}, v_{C_{ds}}) = (A_0 + A_1 v_{G'S'} + A_2 v_{G'S'}^2 + A_3 v_{G'S'}^3) \tanh(\alpha v_{C_{ds}}), \quad (113.a)$$

$$C_{gs}(v_{C_{gs}}) = \frac{C_{gso}}{\sqrt{1 - v_{C_{gs}} / \phi_{bi}}}. \quad (113.b)$$

The parameters used in (113.a) and (113.b) for the example illustrated below were the same as those presented in [58].

The approach used in [58] is based on the voltage-source formulation. The approach used here is based on the current-source formulation. This has proven to be a more convenient approach for implementation, and the same level of accuracy is achieved. Then, from Fig. 22, the state equations are derived as:

$$\dot{v}_{C_{GF}} = (-i_{L_g} + I_{Gate}) / C_{GF}, \quad (114.a)$$

$$\dot{v}_{C_{gs}} = (-v_{C_{gs}} + v_{C_{gd}} + v_{C_{ds}}) \sqrt{1 - v_{C_{gs}} / \phi_{bi}} / C_{gso} R_i, \quad (114.b)$$

$$\dot{v}_{C_{gd}} = (v_{C_{gs}} - v_{C_{gd}} - v_{C_{ds}} + R_i i_{L_g}) / C_{gd} R_i, \quad (114.c)$$

$$\dot{v}_{C_{ds}} = \left(v_{C_{gs}} / R_i - v_{C_{gd}} / R_i - \left(\frac{1}{R_i} + \frac{1}{R_{ds}} \right) v_{C_{ds}} - I_{ds} + i_{L_g} - i_{L_d} \right) / C_{ds}, \quad (114.d)$$

$$\dot{v}_{C_{DF}} = (i_{L_d} + I_{drain}) / C_{DF}, \quad (114.e)$$

$$\dot{i}_{L_g} = [-L_{ds} v_{C_{gd}} - L_d v_{C_{ds}} + L_{ds} v_{C_{GF}} - L_s v_{C_{DF}} - L_{1g} i_{L_g} + L_{2g} i_{L_d}] / L_T, \quad (114.f)$$

$$\dot{i}_{L_d} = [L_s v_{C_{GF}} - L_s v_{C_{gd}} + L_g v_{C_{ds}} - L_{gs} v_{C_{DF}} + L_{1d} i_{L_g} - L_{2d} i_{L_d}] / L_T, \quad (114.g)$$

where several of the quantities are defined in (110). The Jacobian matrix J defined in (97.a) is computed using the forward-finite-difference method [60].

A simulation of a nonlinear transistor or amplifier such as the MESFET using the FDTD or PGY methods would proceed as follows: 1) Set up the DC bias by directly applying DC sources at the gate port and the drain port. Note that the DC sources are ramped up using a half-Gaussian pulse and the FDTD simulation is run until a steady state response is achieved. 2) The AC source is superimposed over the DC source once a DC steady state is reached. 3) The total voltages at the

input and output ports (DC+AC) are calculated. 4) Repeat steps 1-3 but without turning on the steady state response. 5) The AC responses are obtained by subtracting the time responses in step 4 from those computed in steps 1-3.

A nonlinear MESFET amplifier was simulated using the FDTD method. The example is similar to that presented in [58]. The same mesh dimensions used for the linear amplifier (Fig. 22) were used for this case. A 10 cell PML was used on all walls (except for the ground plane) to terminate the mesh. For this example, the DC biasing voltages used were $V_{GS} = -0.81$ V, and $V_{DS} = 6.4$ V. The AC source signal was a modulated Gaussian pulse with center frequency $f_m = 6$ GHz. The amplitude of the source was quite small so that the device was operating in a linear region. Thus, broadband information was extracted. The results of the simulation are illustrated in Fig. 26. It is observed that the device is matched at 6 GHz and has a gain of 12 dB at this frequency. Comparing these results to those published in [58] demonstrates excellent agreement.

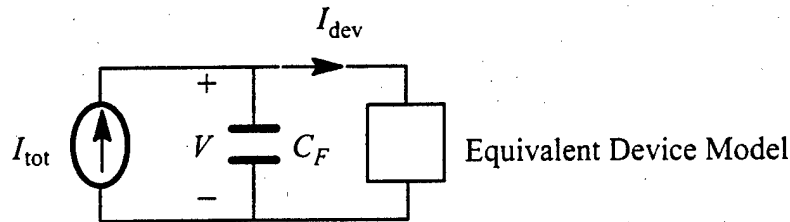


Fig. 20 Equivalent circuit for the current-source state variable model.

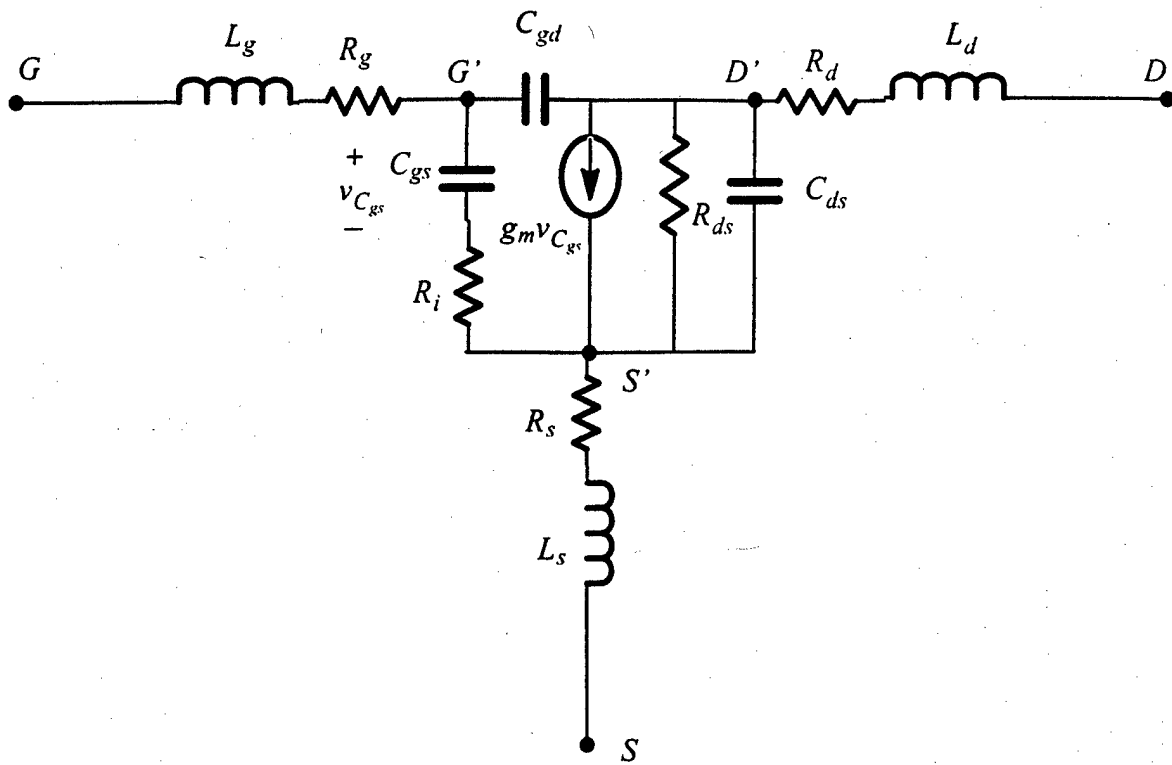


Fig. 21 The small signal equivalent circuit model used for the GaAs MESFET amplifier.

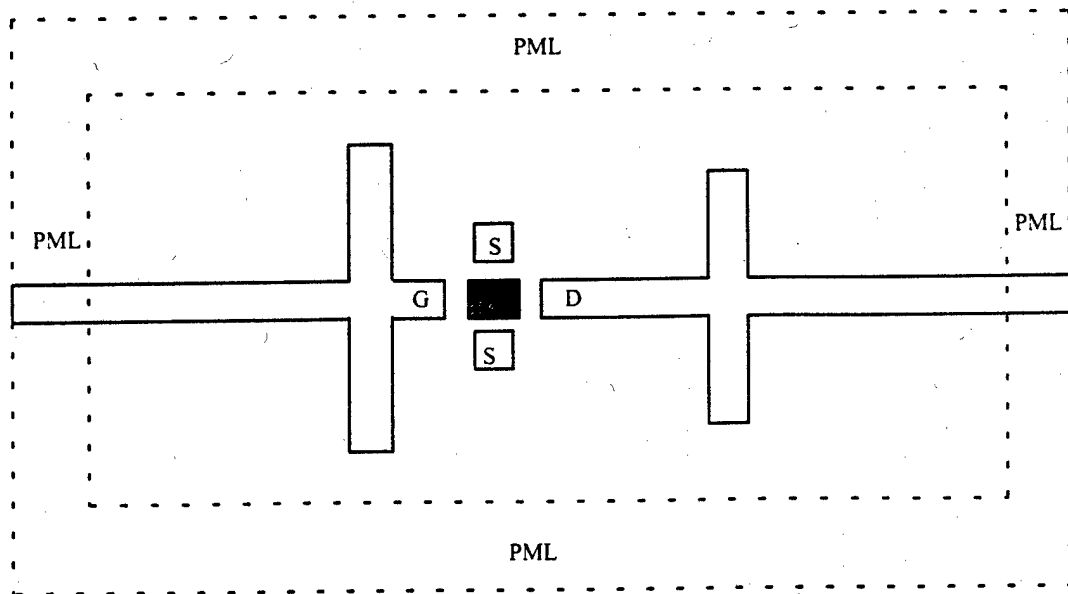


Fig. 22 The layout for the MESFET amplifier. The microstrips have 50Ω characteristic impedances and are printed on a 31 mil substrate with $\epsilon_r = 2.23$. The FDTD model had a spatial discretization of $\Delta x = \Delta y = 0.3000875$ mm, $\Delta z = 0.15748$ mm, and a time step of $\Delta t = 4.011 \times 10^{-13}$ s was used. This lead to 8 cells across the microstrip width and 5 cells through the substrate.

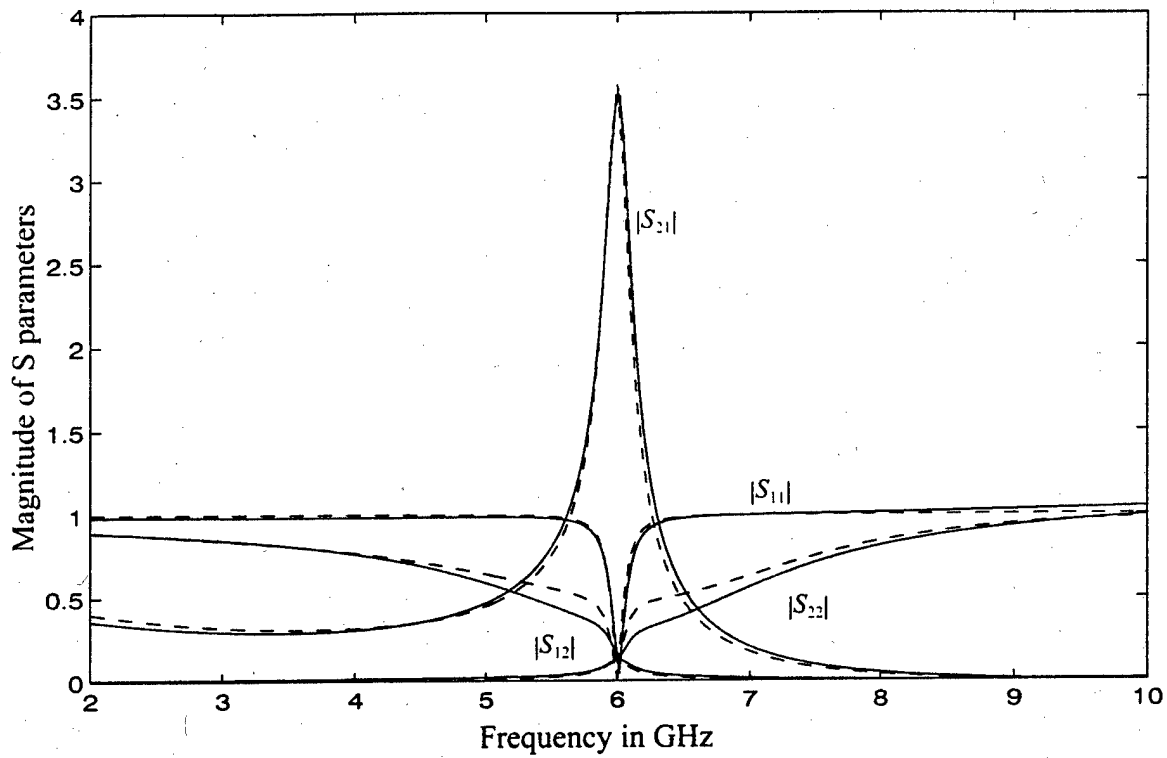


Fig. 23 The magnitude of the S-parameters of the linear MESFET amplifier computed by FDTD with the state-variable model and compared by computations using HP-EESOF™.

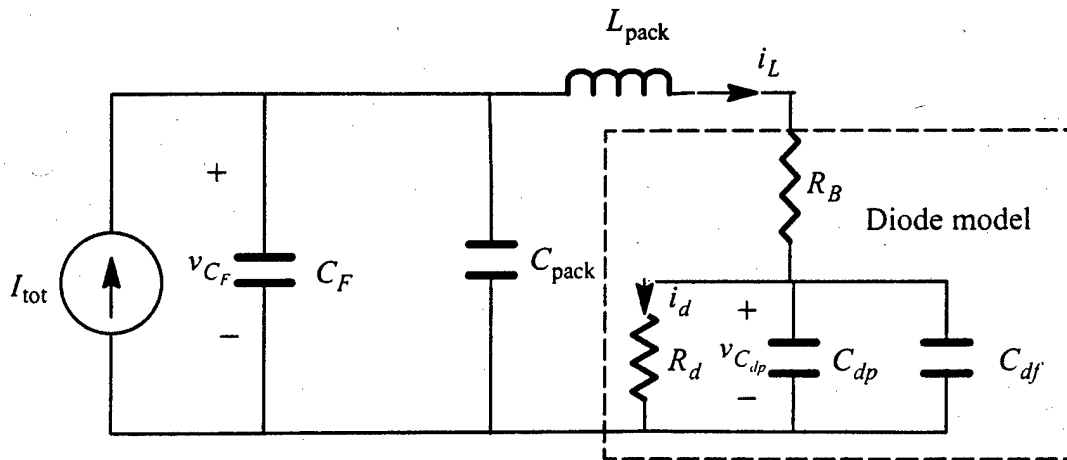


Fig. 24 Equivalent circuit for the diode model. Both C_{pack} and L_{pack} are introduced to model parasitic packaging affects.

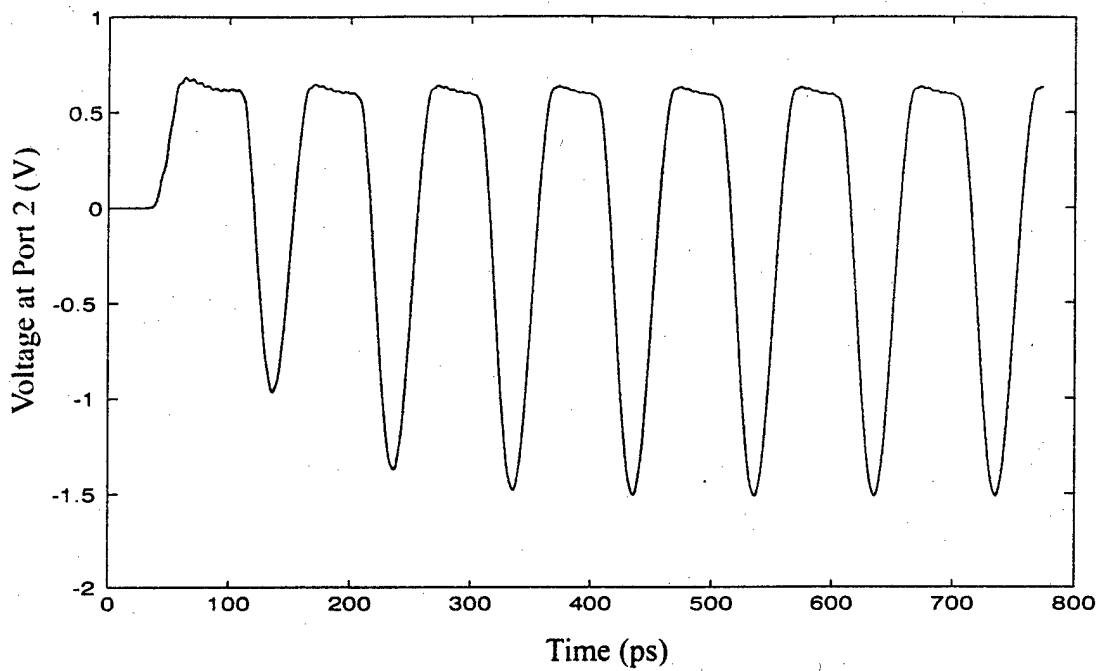


Fig. 25 Voltage across the nonlinear diode terminating a 50 ohm microstrip line.

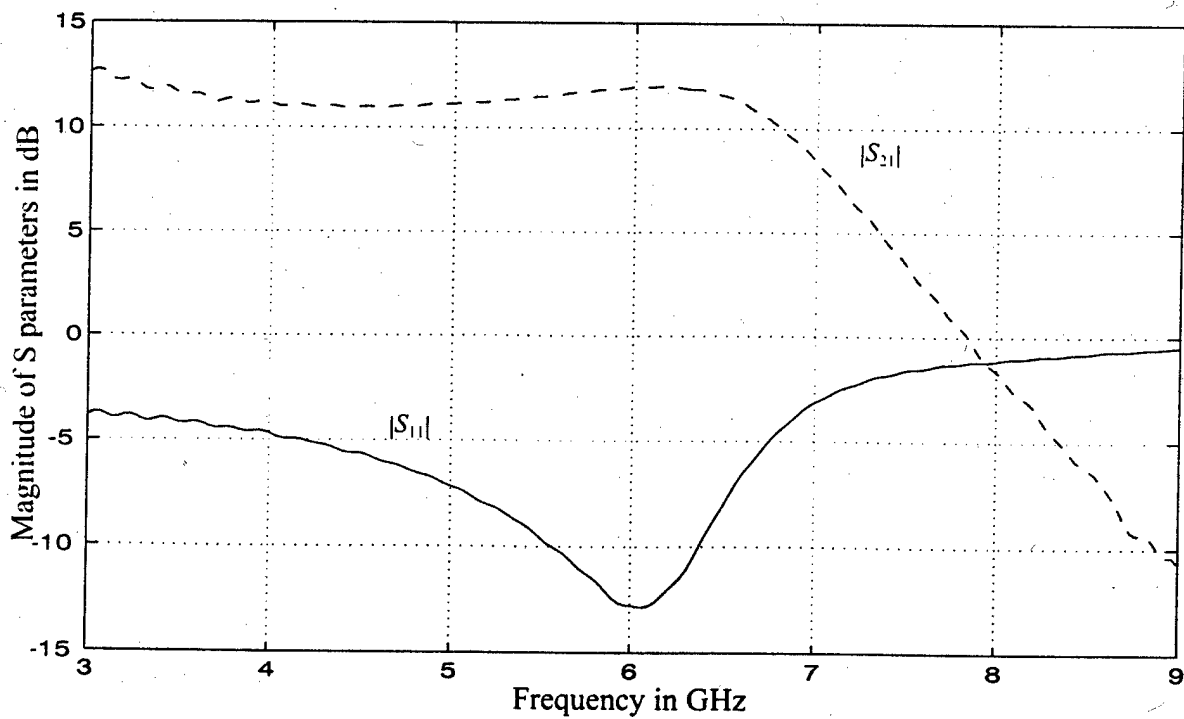


Fig. 26 The magnitude of the S-parameters computed by the FDTD simulation for the nonlinear MESFET amplifier.

6. LIST OF PUBLICATIONS

1. Refereed Journal Articles

The following papers published in refereed journals were supported in whole or in part by ARO Grant# DAAHO4-94-G-0243 with the University of Kentucky.

A. Roden, P. Harms, J. Maloney, M. Kesler, E. Kuster, and S. Gedney, "Time Domain Analysis of Periodic Structures at Oblique Incidence: Orthogonal and Non-Orthogonal FDTD," *IEEE Transactions on Microwave Theory and Techniques*, vol. 46, pp. 420-427, April 1998.

U. Navsariwala, and S. Gedney, "A parallel FETI - Finite Element Time-Domain algorithm for the solution of the time-dependent vector wave equation," *Microwave and Optical Technology Letters*, vol. 16, n. 4, pp. 204-208, November, 1997.

C. T. Wolfe, U. Navsariwala, and S. Gedney "A Parallel Finite-Element Tearing and Interconnecting Algorithm for Solution of the Vector Wave Equation with PML Absorbing Medium," *IEEE Transactions on Antennas and Propagation*, accepted for publication.

J. Alan Roden and Stephen Gedney, "Efficient Implementation of the Uniaxial Based PML Media in Three-Dimensional Non-orthogonal Coordinates Using the FDTD Technique," *Microwave and Optical Technology Letters*, vol. 14, n. 2, pp. 71-75, February 5, 1997.

Stephen D. Gedney, "An anisotropic perfectly matched layer absorbing media for the truncation of FDTD Lattices," *IEEE Transactions on Antennas and Propagation*, vol. 44, pp. 1630-1639, December 1996.

Stephen D. Gedney, "An Anisotropic PML Absorbing Media for FDTD Simulation of Fields in Lossy Dispersive Media," *Electromagnetics*, vol. 16, pp. 399-415, July/August 1996.

Stephen D. Gedney, Faiza Lansing, and Dan Rascoe, "A full-wave analysis of passive monolithic integrated circuit devices using a generalized Yee-algorithm," *IEEE Transactions on Microwave Theory and Techniques*, vol. 44, July 1996.

Stephen D. Gedney and Umesh Navsariwala, "An unconditionally stable implicit finite-element time-domain solution of the vector wave equation," *IEEE Microwave and Guided Wave Letters*, vol. 5, pp. 332-334, October 1995.

Stephen D. Gedney, "Finite-difference time-domain analysis of microwave circuit devices on high performance vector/parallel computers," *IEEE Transactions on Microwave Theory and Techniques*, vol. 43, pp. 2510-2514, October 1995.

Stephen D. Gedney and Umesh Navsariwala, "A comparison of the performance of the finite difference time-domain, finite element time-domain, and planar generalized Yee-algorithms on high performance parallel computers," *International Journal on Numerical Modeling (Electronic Networks, Devices and Fields)*, Vol. 8, pp. 265-276, May-August 1995.

Stephen D. Gedney and Faiza Lansing, "A parallel planar generalized Yee-algorithm for the analysis of microwave circuit devices," *International Journal on Numerical Modeling (Electronic Networks, Devices and Fields)*, Vol. 8, pp. 249-264, May-August 1995.

Stephen D. Gedney, "Mesh partitioning schemes of large unstructured meshes for parallel finite element analysis," *Applied Computational Electromagnetics Society Newsletter*, vol. 10, pp. 40-54, July 1995.

The following manuscripts have been submitted to refereed journals for publication and are still under review

S. K. Mazumdar, J. E. Lupp, and S. Gedney, "Performance modeling of the finite-difference time-domain method on high performance parallel systems," *Applied Computational Electromagnetic Journal* (January 1997)

J. Alan Roden and S. Gedney, "Efficient modeling of good conductors in general curvilinear coordinates," submitted to *IEEE Transactions on Microwave Theory and Techniques* (December 1997)

S. Gedney and J. A. Roden, "Well posedness of non orthogonal FDTD methods," submitted to *IEEE Transactions on Antennas and Propagation* (March 1998).

2. Book Chapters

The following book chapters were supported in whole or in part by ARO Grant# DAAHO4-94-G-0243 with the University of Kentucky.

Stephen Gedney, "The Perfectly Matched Layer Absorbing Medium," in *Advances in Computational Electrodynamics I: The Finite-Difference Time-Domain Method*, Allen Taflove, Ed., Artech House, Boston, MA, 1998.

S. Gedney, J. A. Roden, N. K. Madsen, A. H. Mohammadian, W. E. Hall, V. Shankar, and C. Rowell, "Explicit time-domain solution of Maxwell's equations via generalized grids," in *Advances in Computational Electrodynamics: The Finite-Difference Time-Domain Method*, Allen Taflove, Ed., Artech House, Boston, 1998.

Stephen Gedney, "The Computational Performance of the FDTD Algorithm", in *Finite Difference Time Domain Method for Analysis and Design of Microwave Structures*, IEEE Press, Piscataway, NJ. 1998.

Stephen Gedney and Faiza Lansing, "Explicit Time-Domain Solutions of Maxwell's Equations Using Non-Orthogonal and Unstructured Grids," in *Computational Electrodynamics : The Finite Difference Time Domain Method*, Allen Taflove, Ed., Artech House, Boston, MA, 1995.

Stephen Gedney and Stephen Barnard, "Efficient FD-TD Algorithms for Vector and Multiprocessor Computers," in *Computational Electrodynamics : The Finite Difference Time Domain Method*, Allen Taflove, Ed., Artech House, Boston, MA, 1995.

3. International Symposia

The following papers presented in International Symposia were supported in whole or in part by ARO Grant# DAAHO4-94-G-0243 with the University of Kentucky.

P., Petre, M. Matloubian, R. T., Kihm, and S. Gedney, "Simulation and performance of passive microwave and millimeter wave coplanar waveguide circuit devices with flip chip packaging", *Electrical Performance of Electronic Packaging*, sponsored by the IEEE MTT Society and IEEE CPMT Society, San Jose, CA, 27-29 Oct., 1997.

P., Petre, G. Valley, R. T., Kihm, and S. Gedney, "Simulation of large packaged dense microwave circuits", *Electrical Performance of Electronic Packaging*, sponsored by the IEEE MTT Society and IEEE CPMT Society, San Jose, CA, 27-29 Oct., 1997.

P. H. Harms, A. Roden, J. Maloney, M. Kesler, E. Kuster, and S. Gedney, "Numerical Analysis of Periodic Structures Using the Split Field Update Algorithm", *The Thirteenth Annual Review of Progress in Applied Computational Electromagnetics*, Monterey, CA: March 17-21, 1997.

S. Gedney, "Efficient Implementation of the Uniaxial PML Absorbing Media for Generalized FDTD Methods," *The Thirteenth Annual Review of Progress in Applied Computational Electromagnetics*, Monterey, CA: March 17-21, 1997.

S. Gedney, John Ottusch, Peter Petre, John Visser, and Stephen Wandzura, "Efficient High-Order Discretization Schemes for Integral Equation Methods," *1997 IEEE Symposium on Antennas and Propagation*, Montreal, P.Q., June, 1997.

S. Gedney and F. Lansing, "Advanced FDTD methods on High Performance Parallel Computers," 1996 URSI Radio Science Meeting, Baltimore MD, 1996. (Invited Paper)

S. Gedney and J. A. Roden, "The Uniaxial Perfectly Matched Layer (UPML) Truncation of FDTD Lattices for Generalized Media," 1996 URSI Radio Science Meeting, Baltimore MD, 1996 (Invited Paper)

P. Harms and S. Gedney, "An Unstructured Grid Based FDTD Body of Revolution Algorithm," 1996 URSI Radio Science Meeting, Baltimore MD, 1996.

S. Gedney, F. Lansing, R. T. Kihm, N. Owona and K. L. Virga, "Simulating "Large" Microwave Circuits With The Parallel Planar Generalized Yee Algorithm," *IEEE Symposium on Microwave Theory and Techniques*. San Francisco, CA: 1996.

Stephen D. Gedney and Faiza Lansing, "Implementation of Advanced FDTD methods on Parallel and Distributed Computers," (invited paper) 1995 URSI Radio Science Meeting Digest, Newport Beach, CA June 18-23, 1995.

Stephen D. Gedney and Alan Roden, "Applying Berenger's Perfectly Matched Layer (PML) Boundary Condition to Non-Orthogonal FDTD Analyses of Planar Microwave Circuits," (invited paper) 1995 URSI Radio Science Meeting Digest, Newport Beach, CA June 18-23, 1995.

Umesh Navsariwala and Stephen D. Gedney, "An Implicit Finite Element Time-Domain Method With Unconditional Stability," (invited paper) 1995 IEEE Symposium on Antennas and Propagation Digest, Newport Beach, CA June 18-23, 1995.

7. SCIENTIFIC PERSONNEL

The following personnel have been supported under ARO Grant# DAAHO4-94-G-0243 with the University of Kentucky during the period of 1/96 through 2/97

Stephen D. Gedney:	PI
Paul Harms:	Postdoctoral Scholar
Mehdi Mekaik:	Postdoctoral Scholar
J. Alan Roden:	Ph.D. (Summer 1997)
Umesh Navsariwala:	Ph.D. (Expected Summer 1998)
C. T. Wolfe:	Ph.D. (Expected Fall 1998)
Norbert Owona:	M.S. (Summer 1997) - Research Assistantship
Ling He:	M.S. (Spring 1997) - Research Assistantship
Harikrishna Yelleti:	M.S. (Spring 1998) - Research Assistant

8. REPORT OF INVENTIONS

Not Applicable

9. BIBLIOGRAPHY

- [1] S. Gedney, F. Lansing and D. Rascoe, "A full-wave analysis of passive monolithic integrated circuit devices using a generalized Yee-algorithm", *IEEE Transactions on Microwave Theory and Techniques*, vol. 44, pp. 1393-1400, August 1996.
- [2] S. Gedney, F. Lansing and D. Rascoe, "Full Wave Analysis of Microwave Monolithic Circuit Devices Using a Generalized Yee Algorithm Based on Unstructured Grids", Technical Report NASA Tech Brief# NPO-19186, NASA/JPL, Pasadena, CA, March, 1995.
- [3] S. Gedney and F. Lansing, "Explicit Time-Domain Solutions of Maxwell's Equations Using Non-Orthogonal and Unstructured Grids", *Finite Difference Time Domain Methods for Electrodynamical Analyses*, A. Taflov Ed., pp. New York, NY: Artech House 1995.
- [4] S. Gedney and F. Lansing, "A Parallel Planar Generalized Yee-Algorithm For the Analysis of Microwave Circuit Devices", *International Journal for Numerical Modeling (Electronic Networks, Devices and Fields)*, vol. 8, pp. 265-276, May-August 1995.
- [5] S. Gedney, F. Lansing, R. T. Kihm, N. Owona and K. L. Virga, "Simulating "Large" Microwave Circuits With The Parallel Planar Generalized Yee Algorithm", *IEEE Transactions on Microwave Theory and Techniques*, vol. submitted for review, pp. 1996.
- [6] S. Gedney and U. Navsariwala, "An unconditionally stable implicit finite-element time-domain solution of the vector wave equation", *IEEE Microwave and Guided Wave Letters*, vol. 5, pp. 332-334, October 1995.
- [7] U. Navsariwala and S. Gedney, "An efficient implementation of the finite-element time-domain algorithm on parallel computers using a finite-element tearing and interconnecting algorithm", *Microwave and Optical Technology Letters*, vol. 16, pp. 204-208, November 1997.
- [8] S. Gedney, "Finite-Difference Time-Domain Analysis of Microwave Circuit Devices on High Performance Vector/Parallel Computers", *IEEE Transactions on Microwave Theory and Techniques*, vol. 43, pp. 2510-2514, October 1995.
- [9] S. D. Gedney and U. Navsariwala, "A comparison of the performance of the finite difference time-domain, finite element time-domain, and planar generalized Yee-algorithms on high performance parallel computers", *International Journal on Numerical Modeling (Electronic Networks, Devices and Fields)*, vol. 8, pp. 265-276, May-August 1995.
- [10] S. Gedney and S. Barnard, "Efficient FD-TD Algorithms for Vector and Multiprocessor Computers", *Finite Difference Time Domain Methods for Electrodynamical Analyses*, A. Taflov Ed., pp. Boston, MA: Artech House 1995.
- [11] S. D. Gedney, "The computational performance of the FDTD Algorithm", *Finite Difference Time-Domain Method for Analysis and Design of Microwave Structures*, T. Itoh and B. Houshmand Ed., pp. Piscataway, NJ: IEEE Press 1997.
- [12] S. Gedney, "Mesh partitioning schemes of large unstructured meshes for parallel finite element analysis", *Applied Computational Electromagnetics Society Newsletter*, vol. 10, pp. 40-54, July 1995.
- [13] C. T. Wolfe, U. Navsariwala and S. Gedney, "A Parallel Finite-Element Tearing and Interconnecting Algorithm for Solution of the Vector Wave Equation with PML Absorbing Medium", *IEEE Transactions on Antennas and Propagation*, vol. submitted for review, pp. 1997.
- [14] S. D. Gedney, "An anisotropic perfectly matched layer absorbing media for the truncation of FDTD Lattices", *IEEE Transactions on Antennas and Propagation*, vol. 44, pp. 1630-1639, December 1996.
- [15] S. D. Gedney, "An anisotropic PML absorbing media for FDTD simulation of fields in lossy dispersive media", *Electromagnetics*, vol. 16, pp. 399-415, July/August 1996.
- [16] J. A. Roden and S. D. Gedney, "Efficient Implementation of the Uniaxial Based PML Media in Three-Dimensional Non-orthogonal Coordinates Using the FDTD Technique", *Microwave and Optical Technology Letters*, vol. 10, pp. 71-75, February 1997.

- [17] R. Holland, "Finite-difference solution of Maxwell's equations in generalized nonorthogonal coordinates", *IEEE Transactions on Nuclear Science*, vol. NS-30, pp. 4589-4591, 1983.
- [18] J.-F. Lee, R. Palendech and R. Mittra, "Modeling three-dimensional discontinuities in waveguides using nonorthogonal FDTD algorithm", *IEEE Transactions on Microwave Theory and Techniques*, vol. 40, pp. 346-352, February 1992.
- [19] N. Madsen, "Divergence preserving discrete surface integral methods for Maxwell's equations using nonorthogonal unstructured grids", Technical Report UCRL-JC-109787, LLNL, February, 1992.
- [20] S. D. Gedney and J. A. Roden, "Well posed non-orthogonal FDTD methods", Technical Report EMG-98-01, University of Kentucky, January 1998, 1998.
- [21] B. Gustafsson, H.-O. Kreiss and J. Oliger, *Time-Dependent Problems and Difference Methods*, New York: John Wiley & Sons, 1995.
- [22] L. N. Trefethen, "Lax-stability vs. eigenvalue stability of spectral methods", *Numerical Methods for Fluid Dynamics III*, K. W. M. a. M. J. Baines Ed., pp. 237-253. Oxford: Clarendon Press 1988.
- [23] L. N. Trefethen, "Pseudospectra of matrices", *Numerical Analysis 1991*, D. F. Griffiths and G. A. Watson Ed., pp. 234-266. Essex, UK: Longman Scientific and Technical 1992.
- [24] J. A. Roden, "Broadband Electromagnetic Analysis of Complex Structures with the Finite-Difference Time-Domain Technique in General Curvilinear Coordinates", Ph. D., University of Kentucky, 1997.
- [25] I. Bardi, O. Biro, K. Preis and B. R. Vrisk K. R., "Nodal and edge element analysis of inhomogeneous loaded 3D cavities", *IEEE Transactions on Magnetics*, vol. 28, pp. 1142-1145, Feb. 1992.
- [26] J. P. Berenger, "A perfectly matched layer for the absorption of electromagnetic waves", *Journal of Computational Physics*, vol. 114, pp. 185-200, October 1994.
- [27] W. C. Chew and W. H. Weedon, "A 3D perfectly matched medium from modified Maxwell's equations with stretched coordinates", *IEEE Microwave and Guided Wave Letters*, vol. 7, pp. 599-604, September 1994.
- [28] D. S. Katz, E. T. Thiele and A. Taflove, "Validation and extension to three-dimensions of the Berenger PML absorbing boundary condition for FD-TD meshes", *IEEE Microwave and Guided Wave Letters*, vol. 4, pp. 268-270, August 1994.
- [29] Z. S. Sacks, D. M. Kingsland, R. Lee and J. F. Lee, "A perfectly matched anisotropic absorber for use as an absorbing boundary condition", *IEEE Transactions on Antennas and Propagation*, vol. 43, pp. 1460-1463, December 1995.
- [30] J. Fang and Z. Wu, "Generalized perfectly matched layer - an extension of Berenger's Perfectly Matched Layer Boundary Condition", *IEEE Microwave and Guided Wave Letters*, vol. 5, pp. 451-453, December 1995.
- [31] A. Taflove, *Computational Electrodynamics: The Finite-Difference Time-Domain Method*, Boston, MA: Artech House, 1995.
- [32] J.-P. Berenger, "Perfectly Matched Layer for the FDTD Solution of Wave-Structure Interaction Problems", *IEEE Transactions on Antennas and Propagation*, vol. 51, pp. 110-117, January 1996.
- [33] J.-P. Berenger, "Improved PML for the FDTD Solution of Wave-Structure Interaction Problems", *IEEE Transactions on Antennas and Propagation*, vol. 45, pp. 466-473, March 1997.
- [34] Z. Wu and J. Fang, "High-Performance PML Algorithms", *IEEE Microwave and Guided Wave Letters*, vol. 6, pp. 335-337, September 1996.
- [35] L. He, "FDTD - Advances in subsampling methods, UPML, and higher-order boundary conditions", MS, University of Kentucky, 1997.
- [36] D. Sheen, S. Ali, M. Abouzahra and J. A. Kong, "Application of the three-dimensional finite-difference time-domain method to the analysis of planar microstrip circuits", *IEEE Transactions on Microwave Theory and Techniques*, vol. 38, pp. 849-856, July 1990.

- [37] A. Tulintseff, "The finite-difference time-domain method and computer program description applied to multilayered microstrip antenna and circuit configurations", Technical Report AMT: 336.5-92-041, Jet Propulsion Laboratory, May, 1992.
- [38] R. D. Ferraro, "Solving partial differential equations for electromagnetic scattering problems on coarse-grained concurrent computers", *Computational Electromagnetics and Supercomputer Architecture*, 7, T. C. a. J. Patterson Ed., pp. 111-154. Cambridge, MA: EMW Publishing 1993.
- [39] J. Patterson, T. Cwik, R. Ferraro, N. Jacobi, P. Liewer, T. Lockhart, G. Lyzenga, J. Parker and D. Simoni, "Parallel computation applied to electromagnetic scattering and radiation analysis", *Electromagnetics*, vol. 10, pp. 21-40, January-June 1990.
- [40] R. Lee and V. Chupongstimun, "A Partitioning Technique for the Finite Element Solution of Electromagnetic Scattering from Electrically Large Dielectric Cylinders", *IEEE Transactions on Antennas and Propagation*, vol. 42, pp. 737-741, May 1994.
- [41] B. Després, "Domain decomposition method and boundaries the Helmholtz problem", Proc. Int. Symp. Mathemat. Numerical Aspects Wave Propagat. Phenomena, Strasbourg France, vol. pp. 44-52, 1992.
- [42] B. Després, "A Domain decomposition method and the Helmholtz problem (Part II)", Proc. 2nd International Conference on the Mathematical Aspects of Wave Propagation, Dover, DE, vol. pp. 197-206, 1993.
- [43] B. Stupfel, "A Fast Domain Decomposition Method for the Solution of Electromagnetic Scattering by Large Objects", *IEEE Transactions on Antennas and Propagation*, vol. 44, pp. 1375-1385, October 1996.
- [44] B. Stupfel, "Absorbing boundary conditions on arbitrary boundaries for the scalar and vector wave equations", *IEEE Transactions on Antennas and Propagation*, vol. 42, pp. 773-780, 1994.
- [45] C. Farhart and F. X. Roux, "A method of finite element tearing and interconnecting and its parallel solution algorithm", *International Journal on Numerical Methods in Engineering*, vol. 32, pp. 1205-1227 1991.
- [46] P. B. Monk, "A mixed method for approximating Maxwell's equations", *SIAM Journal on Numerical Analysis*, vol. 28, pp. 1610-1634, December 1991.
- [47] J. T. Elson, H. Sangani and C. H. Chan, "An explicit time-domain method using three-dimensional Whitney elements", *Microwave and Optical Technology Letters*, vol. 7, pp. 607-609, 13 1994.
- [48] C. H. Chan and e. al., "Electromagnetic scattering of waves by random rough surface: a finite-difference time-domain approach", *Microwave and Optical Technology Letters*, vol. 4, pp. 355-358, no. 9 1991.
- [49] M. R. Veysoglu, R. T. Shin and J. A. Kong, "A finite-difference time-domain analysis of wave scattering from periodic surfaces: Oblique incidence case", *Journal on Electromagnetic Waves and Applications*, vol. 7, pp. 1595-1607, no. 12 1993.
- [50] Y.-C. A. Kao and R. G. Atkins, "A finite difference time-domain approach for frequency selective surfaces at oblique incidence", IEEE Antennas and Propagation Society International Symposium, Baltimore, MD, vol. 2, pp. 1432-1435, 1996.
- [51] J. A. Roden, M. P. Kesler, J. G. Maloney, P. H. Harms and S. D. Gedney, "Time-domain analysis of periodic structures at oblique incidence: Orthogonal and non-orthogonal FDTD implementations", *IEEE Transactions on Microwave Theory and Techniques*, vol. in press, pp. 1997.
- [52] J. A. Stratton, *Electromagnetic Theory*, New York: McGraw-Hill, 1941.
- [53] W. Sui, D. Christensen and C. Durney, "Extending the two-dimensional FDTD method to hybrid electromagnetic systems with active and passive lumped elements", *IEEE Transactions on Microwave Theory and Techniques*, vol. 40, pp. 724-730, April 1992.
- [54] M. Piket-May, A. Taflove and J. Baron, "FD-TD modeling of digital signal propagation in 3-D circuits with passive and active loads", *IEEE Transactions on Microwave Theory and Techniques*, vol. 42, pp. 1514-1523, August 1994.

- [55] V. A. Thomas, M. E. Jones, M. Picket-May, A. Taflov and E. Harrigan, "The use of spice lumped circuits as sub-grid models for FDTD analysis", *IEEE Microwave and Guided Wave Letters*, vol. 4, pp. 141-143, May 1994.
- [56] C. N. Kuo, V. A. Thomas, S. T. Chew, B. Houshmand and T. Itoh, "Small signal analysis of active circuits using FDTD algorithm", *IEEE Microwave and Guided Wave Letters*, vol. 5, pp. 216-218, July 1995.
- [57] C. N. Kuo, R. B. Wu, B. Houshmand and T. Itoh, "Modeling of microwave active devices using the FDTD analysis based on the voltage-source approach", *IEEE Microwave and Guided Wave Letters*, vol. 6, pp. 199-201, May 1996.
- [58] C. N. Kuo, B. Houshmand and T. Itoh, "Full-wave analysis of packaged microwave circuits with active and nonlinear devices: An FDTD approach", *IEEE Transactions on Microwave Theory and Techniques*, vol. 45, pp. 819-826, May 1997.
- [59] L. O. Chua and P. M. Lin, *Computer Aided Analysis of Electronic Circuits: Algorithms and Computational Techniques*, Englewood Cliffs, New Jersey: Prentice-Hall, Inc., 1975.
- [60] J. E. Dennis and R. B. Schnabel, *Numerical Methods for Unconstrained Optimization and Nonlinear Equations*, Englewood Cliffs, New Jersey: Prentice-Hall, Inc., 1983.
- [61] W. H. Press, S. A. Teukolsky, W. T. Vetterling and B. P. Flannery, *Numerical Recipes in FORTRAN: The Art of Scientific Computing*, 2nd, New York: Cambridge University Press, 1992.